



**rijksuniversiteit
 groningen**

ZERNIKE INSTITUTE FOR ADVANCED MATERIAL
UNIVERSITY OF GRONINGEN
THE NETHERLANDS

**Ultrafast exciton and charge
dynamics in novel conjugated
oligomers**

Author:

Xiaomeng Liu

S2694743

Supervisors:

Dr. Maxim Pschenichnikov

Dr. Jan Anton Koster

Oleg Kozlov

April 25, 2016

Abstract

Bulk heterojunction (BHJ) organic solar cells (OSCs) based on solution processable organic material have recently attracted much attention for being a very promising alternative to silicon solar cells. The demand for new, more efficient materials has always been one of the main concerns for the organic photovoltaic field. Recently, it was proposed to replace typical OSC materials, conjugated polymers, with organic small molecules (SMs). OSCs based on SM combine advantages of the polymer-based OSCs with such benefits of small molecules as better reproducibility and higher thermal stability. Moreover, because of small molecular weight, vacuum processing of SM-based OSCs is possible, which opens new possibilities for device engineering.

In a constant hunt for best-performing material, a lot of SMs with different chemical structures have been synthesized nowadays. However, alternating of chemical structure of the molecule may lead to unexpected changes of chemical and/or photophysical properties, like decreased charge production efficiency or enhanced recombination. This calls for extensive photophysical studies of each new material.

In this Thesis, early-time photophysics of a novel push-pull small molecule TPA-2T-DCV-Me (TV38) are investigated with steady-state absorption spectroscopy and ultrafast photoinduced absorption (PIA) spectroscopy. To provide a direct connection with OSC operation, charge separation dynamics are investigated in solution-processes TV38:[70]PCBM BHJ and vacuum-deposited TV38/C₆₀ layers.

We found that in mixtures with [70]PCBM acceptor, TV38 acts as well-performing OSC donor material and provide sufficient amount of separated charges. Both *intermolecular* electron transfer from TV38 to [70]PCBM and hole transfer from [70]PCBM to TV38 contribute to the separated charges with comparable fraction. However, the *intramolecular* exciton recombination in TV38 phase and/or recombination of *intermolecular* charge transfer states compete with charge separation process and lead to losses of charges. Overall, BHJ TV38:[70]PCBM blends at the optimized ratio demonstrated that more than 50% of initially generated charges are survived. If these charge lost channels can be suppressed by tuning the blend properties and/or the structure of the molecule, the capability and efficiency for producing long-lived charge will be highly improved.

In layer-structured OSCs, high exciton diffusion distances are required to maximize the exciton harvesting. By employing PIA spectroscopy and analytical modeling, the exciton diffusion distance in vacuum-deposited TV38 is estimated as ~10 nm. This value is in line with the typical exciton diffusion distance in organic material but is much shorter than the light penetration depth in TV38, which is around 80 nm. This rather short exciton diffusion distance significantly limits the exciton harvesting efficiency in the layered structure TV38-based OSCs. Based on the fact that the diffusion distance for TV38 is short, BHJ

architecture seems to be more promising choice for device designing.

In total, the TV38 molecule appears as a promising donor material for OSCs. The results presented in this Thesis provide valuable feedback for device engineers and suggest the ways of further OSCs optimization. The methods presented are universal and applicable for wide range of donor and acceptor materials, and therefore may be utilized for thorough photophysical studies of new photovoltaic compounds (polymers, small molecules and fullerene derivatives).

Acknowledgment

First of all, I offer my sincerest gratitude to my supervisor, Dr. Maxim Pschenichnikov, for offering me this interesting topic and being supportive during my research and thesis writing. I enjoyed all the meetings on Monday mornings, in which we shared our ideas, made plans for the following week and most importantly, I have always been inspired and motivated during the meetings by his comprehensive perspectives and heartfelt encouragements. For sure, I have learnt a lot about physics and chemistry from him, however, what I value more and will benefit from for my life is his way of thinking and enthusiastic attitude when facing unknowns in the research, and that is something I definitely would like to develop in myself.

I also want to thank Prof. Jan Anton Koster from “Photophysics and OptoElectronics” group, for kindly agreeing to be my second supervisor and assessor of my thesis.

I would like to give my special thanks to Oleg Kozlov. Oleg, all the experimental data and data interpretations presented in this thesis would not be possible without the enormous amount of help I had from you. You were always around to help from the first day of me joining our group, whenever I met problems in the lab and no matter how difficult, simple, sometimes even stupid the questions were, you would always explain to me with so much patient. I was lucky to have you supervised me, and have you as a friend.

I would also like to thank our collaborators: Dr. Ponomarenko, Yuriy, Alexander for synthesis the interesting molecule; Dr. Cornil, Dr. Olivier for making the samples..

I wish to thank Foppe de Haan for all the supportive help I had from him, and also for using all the hard- and soft-wares he built, it was actually an amazing experience to see that one person can do so many different things. And prof. Tobey, he gave me the course about lasers and ultrafast spectroscopy and he is the one who actually introduced me to the laser and spectroscopy study.

Thanks to all the colleges who have shared office with me. Joop, I enjoyed all those interesting talks and discussions we had, I am absolutely looking forward to your coming back from U.S. and continuing with our conversations. I want to acknowledge Qi, who has always been nice and helpful, thanks for the discussions and for teaching me to use those software. Björn, I enjoyed the time of being office mate with you. I will always remember the times you tried to improve my Dutch, it really meant a whole lot more than just the language to me. Nilesh, perhaps you could not remember, you gave me the tutorial for the course “Physics of Lasers”, thanks.

Of course I would like to express my gratefulness to the rest members of our OMCP group, Julius- for teaching me climbing and having all the fruitful coffee room discussions. Arthur-for teaching me Russian. Evgeniya-for sharing all the interesting experimental data. Chia Lin- The most important thing I learnt from you is your attitude towards experiments, your “standard experiment procedure” story, I have always kept in mind. Specially, I want to thank Timen, we have attended lectures together, done case study together, been supportive to each other. Timen, you are a great friend.

I have also had a lot help from the people outside our group. Nolan, the first Dutch friend I made. Arsalan, he helped me when I was struggling so much at the very beginning of the life in the Netherland. Miha, Anna, Ellen, Walewein, it is hard to mention you all but all of you guys

made my Dutch living and studying full of joy and meaningfulness.

I want to thank you, Qian, for being so supportive and for sharing all the important moments during the study of my master in the Netherlands.

My dearest friend, Xiaohan, you are the one who encouraged me to come to Europe. And it was you who helped me so much overcome all those obstacles on the way going abroad. Started from teaching me and training me for the English test, to sharing all the valuable experience, to rouse me from hitting the low point, you inspired me to achieve all these. I thank you deeply.

Last but never the least, I would like to thank my parents, who loved me and gave me so many supports for studying in the Netherlands. I never felt fear to difficulties and setbacks because I know you will always stand by my side. I am truly lucky to have you in my life.

Xiaomeng Liu

Groningen

April 2016

Contents

| | |
|--|-----------|
| ABSTRACT | III |
| ACKNOWLEDGMENT | V |
| 1. CHAPTER 1: INTRODUCTION | 1 |
| GENERAL INTRODUCTION | 1 |
| 1.1 WORKING PRINCIPLE OF ORGANIC SOLAR CELLS | 2 |
| 1.1.1 <i>Conjugated molecules</i> | 2 |
| 1.2 CHARGE GENERATION IN ORGANIC SOLAR CELLS | 3 |
| 1.3 BHJ CONCEPT | 4 |
| 1.5 PUSH-PULL APPROACH | 5 |
| 1.6 PHOTOINDUCED ABSORPTION | 6 |
| 1.7 PHOTOINDUCED ABSORPTION SPECTRUM | 8 |
| 1.8 MOTIVATION AND GOALS | 10 |
| 2. CHAPTER 2: CHARGE DYNAMICS IN TV38-BASED BULK HETEROJUNCTIONS | 12 |
| 2.1 INTRODUCTION | 12 |
| 2.2 ABSORPTION SPECTRA | 14 |
| 2.2.1 <i>UV-VIS absorption</i> | 14 |
| 2.2.2 <i>Photoinduced Infrared absorption</i> | 15 |
| 2.3 PHOTOINDUCED ABSORPTION DYNAMICS | 17 |
| 2.4 PHOTOINDUCED ANISOTROPY DYNAMICS | 20 |
| 2.5 EFFICIENCY OF LONG-LIVED CHARGE GENERATION | 21 |
| 2.6 CONCLUSIONS | 22 |
| 2.7 EXPERIMENTAL | 23 |
| 2.8 SUPPLEMENTARY INFORMATION | 25 |
| 3. CHAPTER 3: EXCITON DIFFUSION IN VACUUM-DEPOSITED TV38 HETEROJUNCTION | 30 |
| 3.1 INTRODUCTION | 30 |
| 3.2. ABSORPTION SPECTRA | 32 |
| 3.2.1 <i>UV-VIS absorption</i> | 32 |
| 3.2.2 <i>Photoinduced infrared absorption</i> | 35 |
| 3.3 PHOTOINDUCED ABSORPTION DYNAMICS | 36 |
| 3.4 ANALYTICAL MODEL | 39 |
| 3.5 CONCLUSION | 43 |
| 3.6 EXPERIMENTAL | 44 |
| 3.6.1 <i>Sample preparation</i> | 44 |
| 4. GENERAL CONCLUSIONS AND OUTLOOK | 45 |
| 5. BIBLIOGRAPHY | 48 |
| 6. DECLARATION | 53 |

1. Chapter 1: Introduction

General Introduction

There is a rapidly growing demand for development of renewable and affordable energy sources. The demand stems from the contrast between the enormous energy consumption of Earth's inhabitants and the fact that the reserves of fossil fuel are rather limited.

The Sun delivers its energy to the Earth in various forms, e.g. geothermal, tidal and radiation energy. Among those, solar energy is primarily referring to the radiation energy. The solar energy absorbed by the atmosphere of the Earth, oceans and land is approximately 3850000 exajoules annually [1]. To compare, there was more energy absorbed in one hour than the global human energy consumption in the whole year [2]. Despite the fact that only a half of the incoming solar energy reaches the Earth's surface after being absorbed and reflected by the atmosphere [3], it is still about as much as the energy we will ever get from all of the storage of the Earth's nonrenewable resources [4]. Therefore, energy consumption of human race can potentially be fully supported by solar energy.

To the date, solar energy finally broke the 1% threshold to cover 1% of global electricity demand [5]. The main reason for such a low market share of OSCs is that the current market dominating product - polycrystalline silicon solar cells are relatively expensive if we take into consider the life time and energy consumed in producing , and having environmental unfriendly producing and slow to produce [6-8].

A great deal of scientific research of searching for high-efficient, photovoltaic material have been conducted by researchers all over the world [9, 10]. Amongst all the new materials, organic semiconductors attracted much focus in the past decades [10]. Attractive properties of organic materials like light weight, flexibility, solution-processability etc. allow them to be a promising candidate for alternative to conventional solar cells technology: organic solar cells (OSCs) [11, 12].

All the charge generation processes in OSCs start from the initial dynamics , which occur at ultrafast timescales, including exciton diffusion, exciton dissociation, charge generation and recombination. Hence the initial dynamics are very important to investigate and interpret in order to design a material with sufficient initial charge generation. Also, by studying the ultrafast charge photogeneration processes (generally occur at sub-ns timescales) one is able to provide optimization guidelines for improving the overall OSC efficiency. In this thesis, the photophysical properties of a new organic photovoltaic material on an ultra-fast time scale are investigated, and the ultra-fast charge generation,

transfer and recombination via *inter/intra*-molecular channels are identified.

In this introductory chapter, some important concepts regarding the OSCs photophysics and ultra-fast time resolved spectroscopy are introduced.

1.1 Working Principle of Organic Solar cells

1.1.1 Conjugated molecules

The photovoltaic applicable organic semiconductors are so-called conjugated organic molecules. Conjugated molecules are molecules that are characterized by a backbone chain of alternating double- and single-bonds (Figure 1.1a). Their overlapping p-orbitals create a system which leads to the delocalization of π -electrons along the conjugation chain hence gaining conductivity, optical absorption and a band structure that is similar to inorganic semiconductors [13-15] (Figure 1.1b). The p_z orbitals in such system delocalize and form a bonding π orbital and an anti-bonding π^* orbital. All the delocalized π orbitals form the highest occupied molecular orbital (HOMO) and the π^* orbital is the lowest unoccupied molecular orbital (LUMO). In an organic semiconducting system, HOMO is analog of the valence band and the LUMO on the other hand plays the role of conduction band. The energy offset between LUMO and HOMO is regarded as the band gap of organic semiconducting materials [16]. A simplest example of conjugated molecule can be organic molecule like benzene, fullerenes or carbon nanotubes.

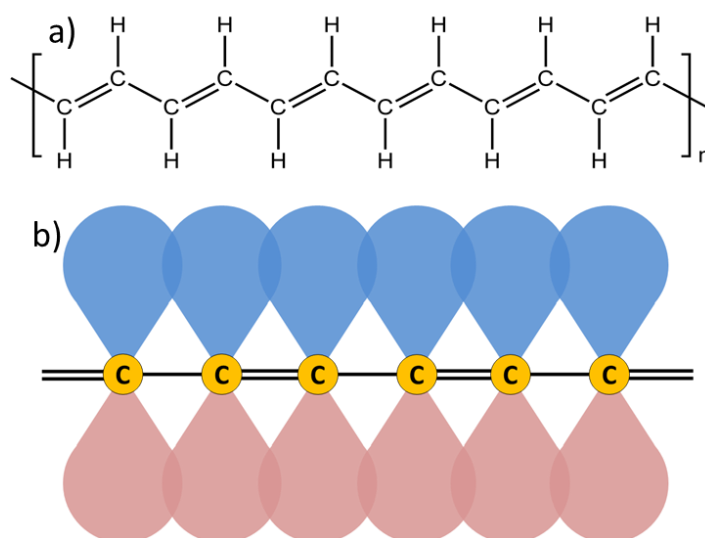


Figure 1.1 a) A structural diagram of *trans*-polyacetylene with a long chain of carbon atoms with alternating single and double bonds between them forming the conjugation [17]. b) Schematic illustration of a conjugated chain. Carbon atoms are shown by yellow circles; solid lines represent single and double bonds while overlapping π -orbitals are shown by blue-red eights.

In the year 2000, the importance of the organic semiconductors was highlighted by awarding the Noble Prize in chemistry to Alan J. Heeger, et. al., "for the discovery and development of conductive polymers" [18, 19].

1.2 Charge generation in organic solar cells

The idea of solar cells is to convert light into electricity, and the converting process in a conventional inorganic solar cell can be briefly described in the following: upon photo excitation of the material in the active layer, free electrons and holes are generated because of a high dielectric constant of the inorganic material. These electrons are excited from HOMO levels to the LUMO levels creating holes on the HOMO levels forming bounded electron-hole pairs. However these bounded electron-hole pairs can be easily separated almost immediately in, e.g. silicon. Then the generated charges are collected at the electrodes and produce photocurrent. However, this is not the case for organic materials. Because of a relatively low dielectric constant of organic materials (typically 3-4) [20], not free charges are formed but highly bound electron-hole pairs (Frenkel excitons) with binding energy of ~ 0.3 eV are created instead [21]. Obviously, this value is much higher than the thermal energy under a room temperature (~ 26 meV for 300K). Hence, in order to dissociate the bounded excitons, extra efforts should be provided by the system. For this reason, energy gradient concept as a very simple yet efficient way to achieve this goal was introduced. Energy gradient can be provided at the interface between donor-type and acceptor-type materials which possessing different work functions (LUMO levels, Figure 1.2)[22]. These energy gradients are large enough to split the excitons [23] and therefore have become the main exciton dissociation method in OSCs. The structure which provides such kind of gradient is called heterojunction. A simplest heterojunction is a bilayer of donor and acceptor materials (planar heterojunction, Figure 1.3a)

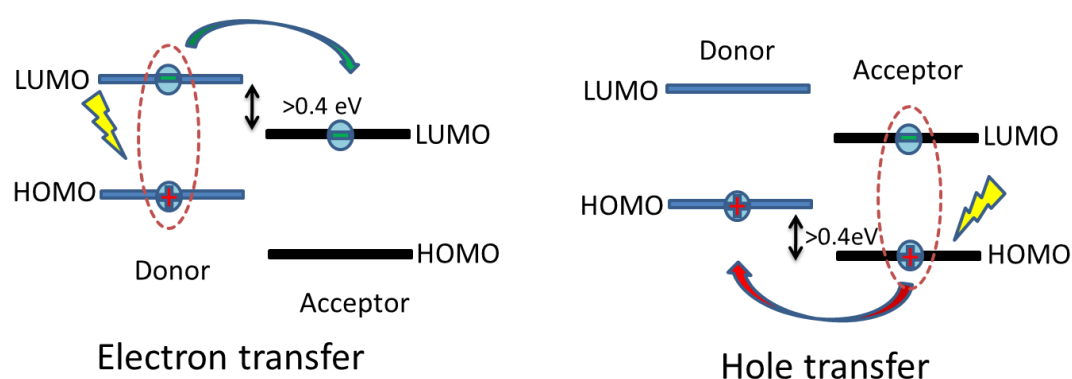


Figure 1.2 Simplified energy band diagram of donor/acceptor blend with photoexcitations (yellow lightning spark), excitons (dashed circles), electron transfer (green arrow) and hole transfer (red arrow).

The charges in organic solar cells can be generated by exciton splitting both from donor phase and acceptor phase. The exciton generated in the donor-type material can be split via electron transfer (ET) to the LUMO level of electron acceptor material [24]. The time scale of ET process is normally in the sub-picosecond range [24]. An example is the extremely high efficiency ET observed in MDMO-PPV/PCBM featuring a less than 50 fs transfer duration [25]. On the other hand, acceptor materials, normally C₇₀ fullerenes and their soluble derivatives, also have significant absorptions in the visible region [26, 27] of the solar spectrum, especially in the blue [28]. The optical excitation of acceptor materials also leads to the formation of excitons, which are similar to the donor excitation. Excitons formed in the acceptor phase can be dissociated via hole transfer (HT) process [29-31]. Therefore the process is essentially driven by the energy gradient of donor/acceptor HOMO-HOMO energy levels.

In the heterojunction systems, the excitons are generated within the bulk of donor (acceptor) materials and have to diffuse to the interface to dissociate. Since the excitons in organic materials have finite lifetime (typically hundreds of ps), and the diffusion coefficient is rather low ($D \sim 10^{-4} \text{ cm}^2/\text{s}$), the exciton diffusion distances are usually around 10 nm [32, 33]. If the exciton is generated far away (>10 nm) from the interface it will simply go to triplet state or recombine via radioactive or nonradioactive pathways not contributing to the separated charges. Therefore, the exciton diffusion length limits the thickness of the donor and acceptor layers in planar heterojunctions to $\sim 10 \text{ nm}$ [34]. On the other hand, to optimize the photon harvesting, the layer thickness should be comparable to the light penetration depth, which is typically a hundred of nm in organic materials [35]. Because of this contradiction, the first planar heterojunction solar cell which was introduced by Tang in 1986 [9] (Figure 1.3a), demonstrated limited efficiency of 1%.

1.3 BHJ concept

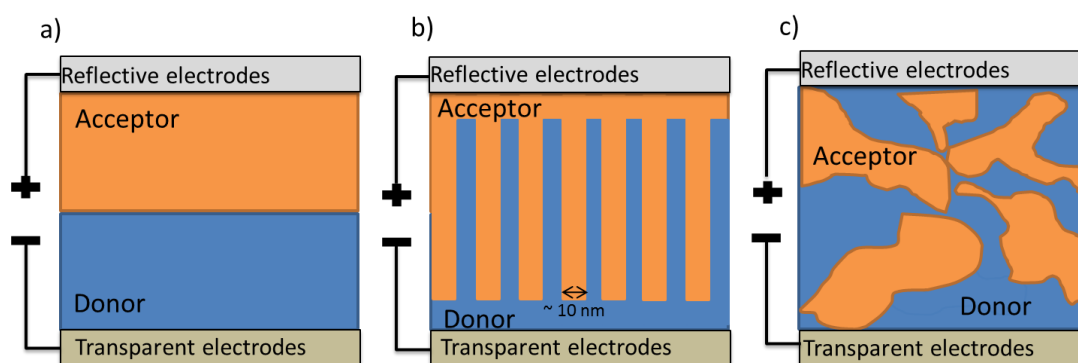


Figure 1.3 Schematic illustration of structure of organic solar cell systems. a) bi-layer structure, b) columnar structure, c) bulk heterojunction structure with a reflective electrode

The contradiction between exciton diffusion and photon harvesting distances limits the efficiency and thus commercial attraction of OSCs. One approach to solve this problem is to enlarge the interfacial area while keeping the capability of excitons to reach the interface (i.e. to create fine separation between donor and acceptor phases). An outstanding idea was to make a vertical columnar structure that as depicted in Figure 1.3b [10].

In such a structure, by introducing an interpenetrating of donor and acceptor material, both of the criteria (sufficient thickness for photon harvesting and fine phase separation for exciton harvesting) are fulfilled. The columns with no more than 20 nm width [36] allow excitons to reach the interface easily while the large vertical layer thickness ensures high light harvesting efficiency. However the feasibility to build such a fine architecture with organic material is rather limited since the assembling of organic material is relatively hard to control [10]. To fabricate this structure with organic material will enormously increase the cost [10], which would dramatically decrease the commercial interest in OSCs [10].

This problem was triumphantly solved by Yu *et al.* in 1995 by introducing the bulk heterojunction (BHJ) concept [22] (Figure 1.3c). In the BHJ, the electron donor and acceptor materials are blended and intermixed in a film with a phase separation scale of few nanometers [37, 38]. The contradiction between light penetration depth and exciton diffusion length is now solved automatically during the self-assembling of BHJ, which thickness can be increased without affecting the phase separation scale. However, since BHJ is a self-assembled system the possibilities to precisely control the structure of the blend are very limited. Therefore, a lot of optimizations on the trial-and-error basis are involved in developing novel BHJ devices. For example, the simplest way to tune the blend structure is to vary the relative amount of donor and acceptor materials in the blend. But in fact, there are still a lot of more advanced approaches in device engineering to achieve the desirable film morphology, i.e. additives, annealing, cast techniques etc. [10]. All in all, the ultimate goal for designing such a device is to obtain a unity efficiency of exciton generation, dissociation and charge collection [10].

1.5 Push-Pull Approach

One of the most important factors that determines the overall efficiency is the sun light absorption efficiency of the OSCs. This can be done by broadening of the absorption spectrum to cover as much as possible of the solar spectrum and by shifting the absorption center to the red to match the solar spectrum hence to obtain the best absorption. For seeking the material that has better absorption property, a lot of novel materials have been introduced in the past decade [39, 40]. Amongst all the material designing approach, a revolutionary designing approach catches our attention, that is the push-pull approach (Figure 1.4a) which was applied to shift the absorption spectrum of the organic material to

the red by reducing the band gap(Figure 1.4b)[41].

In push pull materials, electron-rich units (e.g. triphenylamine or carbazole [42]) are combined with electron-lacking unit (e.g. benzothiadiazole or dicyanovinylene [42]) forming electron donor and acceptor sections. The donor and acceptor units are connected with a conjugated π -bridge (e.g. thienyl, vinyl, or phenyl moieties). The application of this architecture lead to the most promising property--the reduced band gap , which could give a red-shifted absorption and increased light harvesting efficiency. By manipulating the donor and acceptor moieties, the band gap can be controlled [43-46], which gives a lot of opportunities in material engineering.

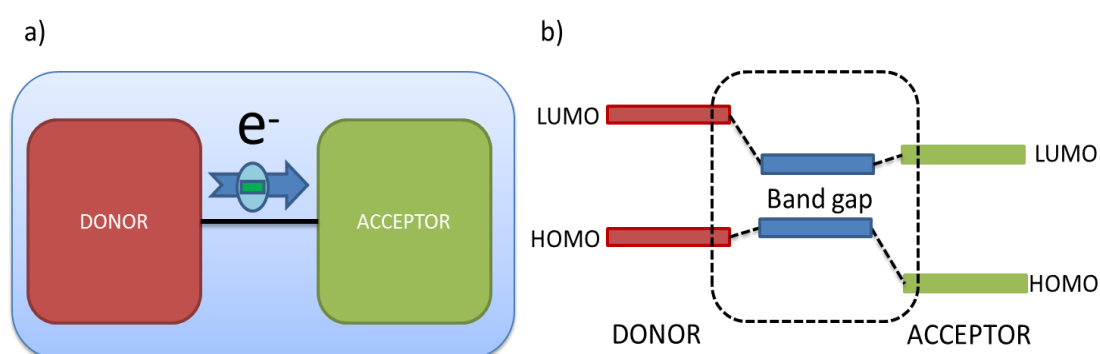


Figure 1.4 (a) Schematic representation of a small molecule with electron donor moiety and acceptor moiety. (b) Schematic of energy levels of the separated moieties (red and green) and the conjugated small molecule (blue). Because of *intra*-molecular interactions, the actual band gap of the whole system is reduced.

A perspective class of donor material possessing a push-pull character is small molecules. This type of material has been of high interest since recently because of several very attractive properties. Like semiconducting polymers, small molecules have the semiconducting behavior due to the delocalization of the π - π electron system[47, 48]. Secondly, as mentioned above, with a push-pull structure they have a notably high absorption coefficients and a red shifted absorption band in the solar radiation spectrum [49-51]. The outstanding property of small molecule, however, is that they are more stable compare to polymer. Small size means relatively easy to synthesis, therefore allowing for batch-to-batch reproduce stability, which potentially reduces the cost of the industrial production. To the date, a 13% efficiency has been obtained with a two-dimensional conjugated small molecule (SMPV1)[52].

1.6 Photoinduced absorption

As mentioned above, all the charge generation processes in OSCs start from the initial

ultrafast dynamics, If no enough charge are generated in the very beginning, then no overall efficiency can be achieved at all, therefore it is very important to study the initial steps of charge generation on the organic material. A good way to investigate these processes is by using time-resolved photoinduced absorption technique.

It is well known that charge doping of organic systems leads to local distortions of molecules and redistributions of charge densities [53]. The coupled charge and local distortions are known as polarons. Polarons are able to propagate along the conjugated chain [54] and eventually contribute to the OSC photocurrent. Due to the polaron-introduced local distortions of the conjugated molecule, the modification of the energy levels occurs. After photoexcitation, an electron is excited from HOMO level to the LUMO level and transferred to the acceptor phase, leaving a vacation (hole) on the HOMO level. Now the HOMO level is singly occupied, which can be regard as a surplus positive charge on the donor phase. These surplus positive charges on the donor phase will intervene the donor electronic structure and introduce an additional absorption band, which has the absorption that normally located in the near and middle infra-red regions [56] in the IR region [55, 56] (Figure 1.5). These absorption bands are called high-energy (HE) and low-energy (LE) polaron absorption bands (Figure 1.5). Since these absorption bands are intrigued by the initial photoexcitation, therefore the polaron absorption is also referred as photoinduced absorption (PIA). PIA spectroscopy is the technique widely used in studying charge dynamics processes. Normally the samples are first excited with an optical pump pulse, and then the PIA is detected with a subsequently following probing pulse (see Time-resolved spectroscopy section for details).

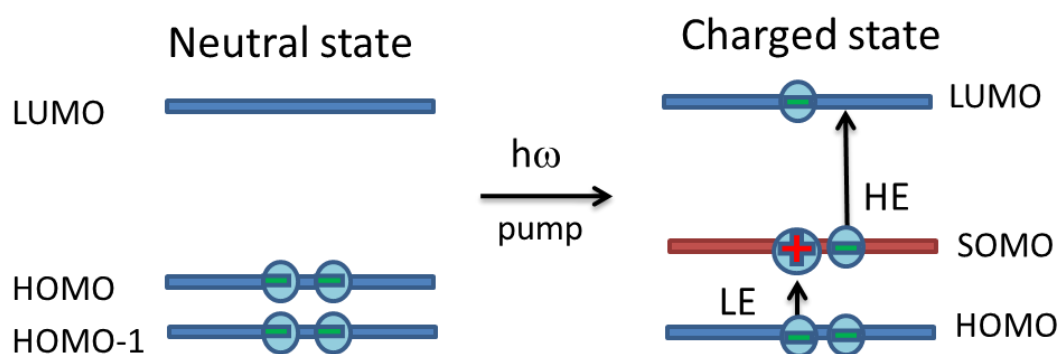


Figure 1.5 Pictorial sketch of the energy levels of a molecule in neutral state and in charged state. Balls with 'minus' and 'plus' signs stand for electrons and hole respectively. HE and LE represent high energy polaron absorption and low energy polaron absorption. Pump is normally optical excitation. The former HOMO level becomes lowest singly occupied level (SOMO).

Even though the charges can be tracked both in HE and LE polaron bands, LE band

have a number of advantages over the HE band. First, it offers contamination free and background free detection of photoinduced absorptions. There is barely observed overlapping between LE band and stimulated emission, triplet-state excitation or ground state bleaching [57], which are often found overlapping with HE absorptions. Second, LE absorption usually does not overlap with any ground-state vibrational absorptions. Another feature makes polaron absorption band a very promising candidate for PIA detection is that the polarization orientation of LE transition dipole moment is strongly correlated with the polarization of charge dipole moment induced by exciting optical pump [58]. With time, due to charge redistribution in the donor phase, the orientation of initial pump-induced dipole moments should be disturbed and all the memory of polarization will be lost eventually. Since the LE transition dipole moment is correlated with this pump-induced polarization, charge transfer dynamics can be tracked by the polarization-sensitive photoinduced absorption spectroscopy, which also works as supplementary information for the isotropy (population) measurements.

1.7 Photoinduced Absorption Spectrum

Time-resolved spectroscopy is a technique specialized in detecting materials in non-equilibrium states. By tracking the evolution (dynamics) of photoinduced non-equilibrium states, time-resolved spectroscopy is able to provide information of how the material "talk to", or interact with its neighboring environment on a micro scale, and by studying non-equilibrium states, one can obtain more insights of equilibrium states.

One of the most widely used time-resolved measurements is optical pump-probe technique [42]. In such measurements, the sample is first optically excited into a non-equilibrium state, and then the following evolution towards equilibrium state is tracked with a time-delayed optical probe. The optical pump and probe are generally ultra-fast laser pulses.

In case of OSCs, the non-equilibrium state is the collection of photoinduced states like excitons or polarons (charges), so that they can be detected optically by exciton or polaron absorption. The probe signal is obtained by measuring of the intensity differences of transmitted probe pulses. When the sample is excited, extra absorption bands are created as described above, and therefore the intensity of transmitted probe pulse is reduced compare to the intensity measured in ground state. In the simplest case, the polarization of the probe pulse is rotated by 54.7° ("the magic angle") [59] with respect to the excitation pulse. In this case, the amount of intensity reduction, which is recorded as ΔT_{iso} , is actually proportional to the population of the photoinduced species:

$$\Delta T_{\text{iso}} \propto N(t) \quad (1)$$

The decay of signal amplitude inherently reflects the temporal evolution of the photoexcited species.

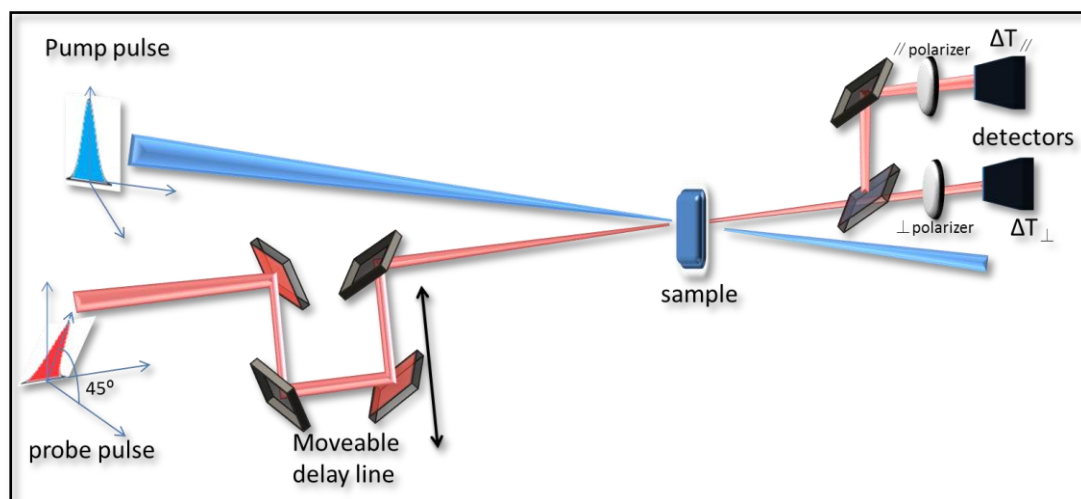


Figure 1.6 Schematic illustration of the PIA experiment: blue and red arrows represent optical excitation (pump) and time-delayed detection (probe), overlapping on the sample; transmission of probe light, which is split into parallel to the excitation and perpendicular to the excitation components are detected separately. ΔT stands for relative transmission change of the probe, which is proportional to photoinduced charge concentration.

The measurement of depolarization can also be a powerful tool in studying OSCs. To obtain the depolarization dynamics, time-resolved photoinduced anisotropy can be tracked. In this case, the components of PIA signal parallel and perpendicular to the polarization of the excitation pulse are recorded independently (Figure 1.6). The isotropic (population) signal and photoinduced anisotropy are recalculated from parallel and perpendicular components of the signal as [59]:

$$\Delta T_{\text{iso}}(t) = \frac{\Delta T_{\parallel}(t) + 2 \times \Delta T_{\perp}(t)}{3} \quad (2)$$

$$r(t) = \frac{\Delta T_{\parallel}(t) - \Delta T_{\perp}(t)}{3 \times \Delta T_{\text{iso}}} \quad (3)$$

In organic systems, rotation of the photoinduced transition dipole moments due to the exciton/charge migration and isotropic hole transfer process are common reasons for signal depolarization. In anisotropy measurements, this depolarization can be readily resolved thus revealing information about charge migration. The rate of depolarization depends on the intra-/inter-molecular interactions therefore very helpful to distinguish these processes.

1.8 Motivation and Goals

Good donor material with properties such as easy synthesis, strong and broadband absorption, and high conductivity is always in demand. One approach for donor material design discussed above is the so-called push-pull approach. Previously, the symmetrical star shaped small push-pull molecule $N(\text{Ph-2T-DCV-Me})_3(2\text{T})$ was thoroughly investigated, and the OSCs with efficiency close to 6% have been fabricated [60, 61]. Intriguingly, the synthesis of 2T molecule can be even further simplified [62] by eliminating the **tree-arm** molecule arrangement. This results in new small molecule TPA-2T-DCV-Me (called TV38 further on) with the broken molecular symmetry (Figure 1.7). The molecule was synthesized by the group of prof. S. Ponomarenko in the Institute for Synthetic Polymer Materials of the Russian Academy of Science, Moscow, Russia [60]. The new asymmetrical molecule TV38 is more promising for having potentially large volume productivity due to the simplified synthesis, which is directly equivalent to high proficiency. Also because of a small size, TV38 is able to withstand both vacuum-deposit processing and solution processing.

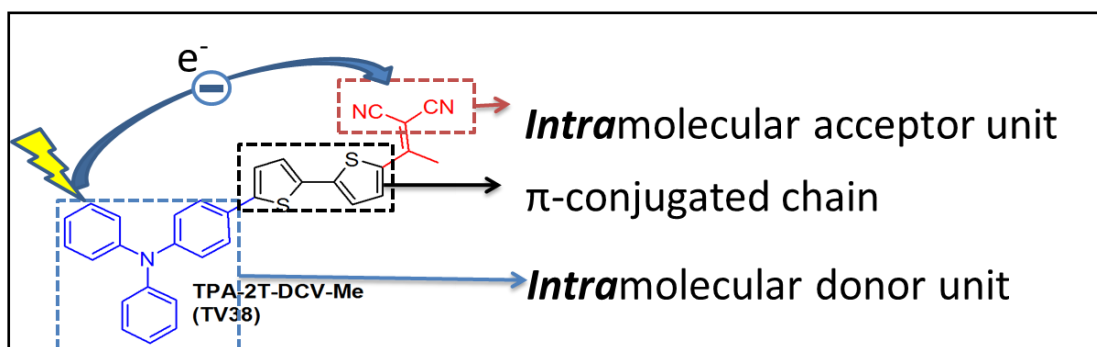


Figure 1.7 Chemical structure of TV38 molecule. Yellow lightning stands for optical excitation. Blue arrow indicates electron transfer from *intramolecular* electron donor unit (blue) to *intramolecular* acceptor unit (red).

If there is not enough charge generated in the very beginning at the ultra-fast time scale, then no overall efficiency can be achieved at all, thus the initial charge dynamics largely determine the overall efficiency of OSCs. Therefore it is very important to understand the photophysical properties of the particular organic donor material on an ultra-fast time scale. Therefore, detailed knowledge of competing charge generation and charge and (or) exciton recombination channels is required for both arrangements proposed.

In BHJ systems, the generation of separated charges is largely determined by the particular blend composition. At the optimal donor: acceptor ratio, the exciton dissociation efficiency is maximized, while the impact of loss channels is minimized. The goals of chapter

2 of this thesis are: i) to determine the charge generation and recombination pathways in BHJs based on TV38; and ii) based on efficiency long-lived charge generation, estimate the optimal blend composition for BHJ OSC based on TV38.

In vacuum-deposited planar heterojunction OSCs, the efficiency is mainly determined by the interplay between light penetration depth of the absorber and the exciton diffusion length in it. The goal of the chapter 3 of this thesis is to measure the exciton diffusion length in vacuum-deposited TV38 layer and compare it with the light penetration depth to estimate the perspectives of TV38-based layered solar cells.

To achieve the goals, ultrafast time resolved spectroscopy was employed.

The optimal blend ratio of TV38:[70]PCBM of 1:4 was found in the BHJ samples. With this optimized blend ratio, more than 50% of initially generated charges are survived within our experimental time window. The main loss channel on the ultra-fast time scale is the *intramolecular recombination*. In this regard, the presumable way of largely increase the efficiency of this OSC system is to suppress this loss channel.

The exciton diffusion distance was estimated to be around 10 nm in the TV38 phase, which is rather short compare to the light penetration depth in the TV38(around 80 nm). The efficiency of bilayer structure OSC base on TV38 will be significantly limited by the short exciton diffusion distance. In this respect, the BHJ structure is most suitable for device engineering.

In total, the small molecule appears as a promising donor material for OSCs. The results presented in this Thesis provide a detailed perspective into the key factors that determine the efficiency of the OSCs and valuable feedbacks for device engineers suggesting the ways of further OSCs optimization.

The methods presented are universal and applicable for wide range of donor and acceptor materials, and therefore may be utilized for thorough photophysical studies of new photovoltaic compounds (polymers, small molecules and fullerene derivatives).

2. Chapter 2: Charge Dynamics in TV38-based Bulk Heterojunctions

This chapter provides the investigation of bulk heterojunction thin films based on TV38: [70]PCBM. Main charge generation and recombination channels are determined as well as the optimized blend ratio. Experimental details and sample preparation is also included.

2.1 Introduction

Solution-processable bulk heterojunction (BHJ) organic solar cells (OSC) have recently attracted much attention as perspective photovoltaic devices which combine semiconducting behavior with benefits of organic materials [51, 63-67]. A typical organic BHJ solar cell consists of a phase-separated mixture of conjugated polymer as electron donor material and the fullerene derivative phenyl-C₆₀-butyric acid methyl ester (PCBM) or phenyl-C₇₀-butyric acid methyl ester ([70]PCBM) with higher absorption coefficient, electron mobility and hole-transfer efficiency [42, 68, 69]. However, it was recently revealed that the polymers in OSCs can be replaced with small molecules (SMs) [49, 70-72]. SMs-based OSCs combine advantages of polymer OSCs like flexibility, solution processability, etc., while they also have their own benefits, for example, high purity, batch-to-batch reproducibility, well-defined molecular structure and molecular weight and easy mass-scale production [20, 48, 73, 74].

Recently it was shown that star-shaped architecture of SMs with triphenylamine (TPA) donor core and dicyanovinyl (DCV) acceptor end groups leads to improved solubility, better layer-to-layer stacking in film and increased number of pathways for the light conversion [23, 75]. It was demonstrated that these star-shaped molecules (SSMs) exhibit fascinating photophysical properties even at ultrafast timescales [23]. For example, it was shown that fast depolarization of the degenerated excited state [76] occurs at ultrafast picosecond timescale, which is followed by efficient intramolecular charge recombination [23]. This unusual behavior can be attributed both to the high symmetry of the molecule and to the particular molecular structure and donor/acceptor units used [23, 47].

To simplify the synthesis procedure and to achieved higher molecular thermal stability, and also, to exclude the effects of molecular symmetry, new molecule TPA-2T-DCV-Me (TV38), was synthesized (Figure 2.1a), which is a non-symmetrical analogue of the N(Ph-2T-DCV-Me)₃ (T2) molecule (Figure 2.1b). In this molecule, the symmetry is broken, and effects like orbital mixing and interactions of arms via shared donor core are eliminated. The direct comparison of photophysical properties of TV38 and T2 molecules allow us to separate the symmetry- and structure-related effects.

In this study, ultrafast dynamics of charge separation and recombination processes were investigated in BHJ thin films based on TV38 with [70]PCBM acceptor (Figure 2.1c) and in TV38 molecules diluted in PMMA matrix. Energy offsets between the TV38 and [70]PCBM energy levels allows both efficient electron transfer from TV38 to [70]PCBM and hole transfer from [70]PCBM to TV38 molecule (Figure 2.1d), and contribution of both processes to charge separation was studied. Time-resolved polarization-sensitive visible-pump IR-probe photoinduced absorption (PIA) spectroscopy was employed to demonstrate the early-time (<2ns) exciton and charge dynamics with femtosecond time resolution.

From the PIA experiments, it was demonstrated that *intramolecular* dynamics of TV38 molecule is very similar with the ones in a symmetric T2 molecule, and therefore is likely attributed to the donor-acceptor combination used. In contrast, ultrafast polarization roots from particular structure of the molecule: in the T2-based films it is both due to charge redistribution and molecular packing while in the TV38-based films only packing plays important role. Finally, it was demonstrated that the TV38-based blends are mostly fullerene-driven due to, most probably, largely blue-shifted blend absorption of [70]PCBM (480 nm and 390 nm) when compare to the neat TV38 absorption (520 nm), and blends provide up to 60% percent of long-lived charges at the optimal TV38:[70]PCBM ratio.

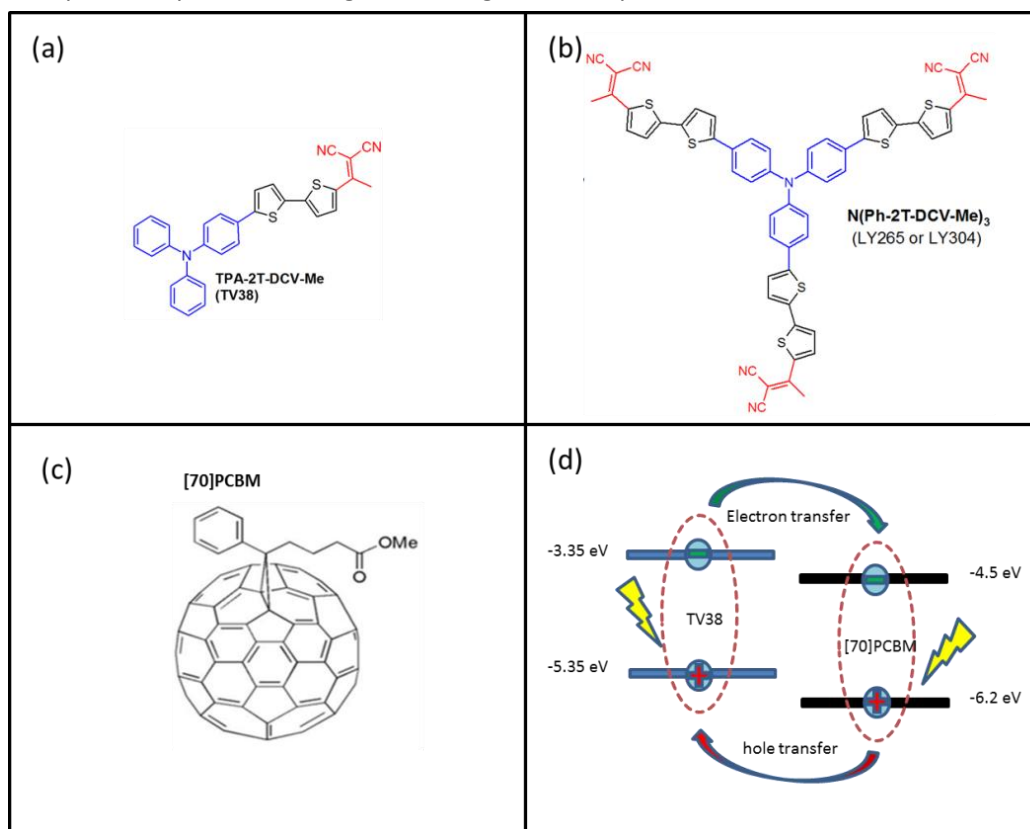


Figure 2.1. Chemical structures of TV38 (a) and T2 (b) small molecular donors and [70]PCBM (c) electron acceptor. (d) Frontier energy levels of TV38 and [70]PCBM. The processes of electron and hole transfer depicted by arrows.

2.2 Absorption Spectra

2.2.1 UV-VIS absorption

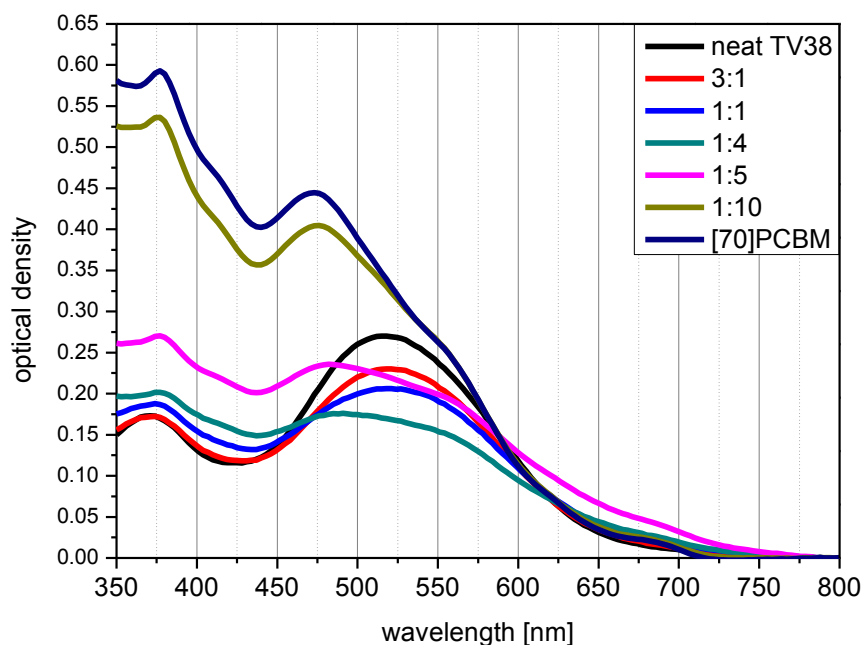


Figure 2.2. Absorption spectra of all blended films with different TV38:[70]PCBM weight ratios (indicated).

Linear absorption spectra of the blends studies are shown in Figure 2.2. Neat TV38 film exhibit two prominent absorption peaks located at ~ 365 nm and ~ 519 nm. Similarly with the T2 SSM [23], the strong peak at 519 nm is assigned to intramolecular charge transfer [23, 76, 77], while the blue peak at 365 nm can be ascribed to the excitation of conjugated backbone as well as the combination of these two above effects [76]. Note that intermolecular interactions in the solid film also affect the absorption peak position and red-shift the absorption spectrum (SI 2).

In the blends, both amplitude and position of the green peak at 519 nm changes with increasing of [70]PCBM concentration. This is due to the fact that [70]PCBM has a different absorption with first maximum located at around 475 nm, and absorbs much less at 519 nm in comparison with TV38. Therefore, in blends with high [70]PCBM concentration, the peak is blue-shifted due to the high contribution of [70]PCBM absorption. In the later PIA measurements, pump wavelength was set at the TV38 absorption maximum of 519 nm.

In the region of 630 nm–720 nm, the TV38:[70]PCBM blends demonstrate prominent absorption shoulder even though the neat TV38 and [70]PCBM films are almost transparent in this region (Figure 2.2). This indicates that the origin of this growth in absorption cannot be simply assigned to a linear combination of TV38 and [70]PCBM absorption. To

demonstrate this effect directly, a tentative linear decomposition of the blend spectra to TV38 and [70]PCBM contribution was performed (SI 1).

Indeed, the blend absorption spectra cannot be fully reconstructed as linear composition of TV38 and [70]PCBM spectra. In the measured spectra, red shifts can clearly be seen compared to the linear decomposition. This indicates the possible formation of ground-state charge-transfer complexes (CTCs) between TV38 and [70]PCBM phase which leads to the decreased band gap and thus to the red shifted absorption [78].

The low-energy absorption band of TV38 is blue-shifted as compared to the star shaped molecule T2 [23]. To be more specific, the absorption maximum of TV38 locates at 519 nm while for star shaped molecule it locates at 530 nm. The reason could be that in a conjugated system the band gap decreases with increasing of the conjugation length. In principle, the nitrogen atom in the center of TPA core breaks the conjugation between the arms in the SSM. However if the nitrogen allows for partial conjugation, the effective conjugation length in SSM would be increased compared to TV38, therefore leading to a red-shifted absorption [23]. Moreover, the particular configuration of the conjugated arms (e.g. the floppiness of the arms) affects the interaction between donor core and each acceptor section, which also could lead to variations in absorption.

2.2.2 Photoinduced Infrared absorption

In order to investigate charge separation dynamics, IR photoinduced absorption (PIA) has been employed. In a conjugated molecule, photogenerated charges create an additional absorption band in the near IR region (the so-called polaron absorption band), and this absorption is proportional to the population of the photogenerated charges [23, 56]. Therefore, by studying the temporal evolution of polaron absorption, the dynamics of photogenerated charges can easily be tracked. One of the most efficient methods to investigate this multi-step dynamic process is pump-probe arrangement.

In conjugated polymers, the near-IR absorption bands are normally located at $1\mu\text{m}\sim 3\mu\text{m}$. The so-called “high-energy polaron absorption band” is located around $1\mu\text{m}$, and the low-energy polaron absorption band is placed around $3\mu\text{m}$ [79]. However, due to the shorter conjugated length of small molecules compared to conjugated polymers, the low-energy band is supposed to be different, and it was indeed observed to be $1.6\mu\text{m}$ for the star shaped molecule T2 [23].

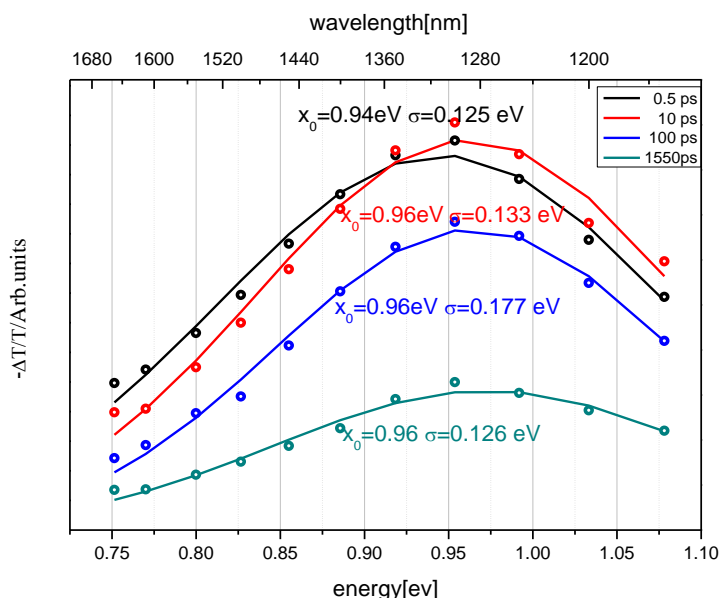


Figure 2.3 PIA spectra of the 1:1 TV38:[70]PCBM blend at different delays. Symbols represent experimental data, solid lines are the fits of experimental data with Gaussian functions. Fitting parameters are indicated next to the curves. Excitation and probe wavelengths were set at 520 nm and 1.3 μm , respectively

Figure 2.3 shows the photoinduced IR absorption spectra of the 1:1 TV38:[70]PCBM blend at different pump-probe delays. The spectra are reconstructed from the transients that were measured at different probe wavelengths. The photoinduced absorption peak is located around 1.3 μm . Note that the red-shift of about 0.02 eV occurs within the first 10 ps. Similar behavior was observed in the spectrum of charge-transfer (CT) excitons in pristine film of TV38 as shown in SI 5. A clear and persistent blue shift and narrowing of the CT-exciton spectrum exists through the whole experimental time window (~ 2 ns) due to e.g. transient polarisability of the environment. The dynamical changes of the polaron spectrum of the blend are due to the residual signal of CT excitons, which are likely split by 10 ps, where the spectrum is stabilized. Since the spectral dynamics are very minor in blended films, single probe wavelength was set at the polaron absorption maximum of 1.3 μm .

If we assume that the only difference between TV38 and star shaped molecule is that the latter has three arms and TV38 has only one, and each arm has exactly the same conjugated length, this will result in a similar band gap and a similar polaron absorption. Surprisingly, this is in sharp contrast with experimentally observed polaron peak for TV38, which is blue shifted compared to the polaron peak of T2 molecule located at 1.6 μm [23]. This can be intuitively understood as discussed previously in the “Visible Absorption” section. In the star shaped molecule, conjugation between two arms is actually not fully broken by the nitrogen atom in the center core of TPA, interactions between adjacent arms via the nitrogen atom can thus lead to a longer over all conjugated length than that of TV38

molecule, and eventually give a red shifted absorption. The other possible explanation of the blue-shift of the polaron spectrum is different interactions of the donor core with the acceptor end group(s). The TV38 molecule consist of one donor core and one DCV acceptor unit, while in T2 the core unit is shared among three acceptor and groups. Since the polaron absorption is very sensitive to the combination of donor and acceptor groups [60], this effect can lead to the substantial changes in the polaron peak position.

2.3 Photoinduced Absorption Dynamics

Figure 2.4 shows the PIA isotropic transients of TV38 with different fullerene loadings. The amplitude of the PIA signal is proportional to the concentration of charges in the blends and the absorption cross-section. The transients were normalized by the film absorption to obtain the relative value of generated charge per absorbed photon. The maximal amplitude amongst the transients was assigned to the unity charge yield. To allow quantified study, all transient dynamics were fitted with the following multi-exponential function

$$\Delta T_{\text{iso}} = A_0 + A_1 \exp\left(-\frac{t}{\tau_1}\right) + A_2 \exp\left(-\frac{t}{\tau_2}\right) + A_3 \left(1 - \exp\left(-\frac{t}{\tau_3}\right)\right) \quad (4)$$

Convolved with a Gaussian apparatus function with standard deviation of $\sigma \approx 100$ fs. In the function, A_i represents the amplitude of the decay component with a lifetime τ_i while A_0 stands for the offset at the end of the transients. All fitting parameters are listed in Table 1.

Table 1 Fit parameters (equation (1)) for pristine film and blends with [70]PCBM

| blends | Offset A_0 | A_1 | τ_1 [ns] | A_2 | τ_2 [ns] | A_3 | τ_3 [ns] | $\sum A_i$ |
|----------|--------------|-------------|---------------|-------------|---------------|-------------|---------------|--------------|
| pristine | 0.32+/-0.09 | 0.12+/-0.01 | 136+/-8 | 0.32+/-0.02 | 1.2+/-1 | - | - | 0.67+/-0.12 |
| 3:1 | 0.36+/-0.1 | 0.07+/-0.01 | 101+/-20 | 0.29+/-0.03 | 0.5+/-0.1 | - | - | 0.73+/-0.14 |
| 1:1 | 0.28+/-0.02 | - | - | 0.31+/-0.03 | 0.7+/-0.1 | 0.12+/-0.05 | 2+/-0.3 | 0.0.81+/-0.1 |
| 1:2 | 0.29+/-0.11 | - | - | 0.37+/-0.05 | 0.4+/-0.1 | 0.2+/-0.03 | 2+/-2 | 0.85+/-0.19 |
| 1:4 | 0.29+/-0.08 | - | - | 0.42+/-0.09 | 0.5+/-0.1 | 0.28+/-0.02 | 6+/-1 | 1+/-0.18 |
| 1:10 | 0.07+/-0.02 | | | 0.15+/-0.03 | 0.6+/-0.1 | 0.2+/-0.06 | 10+/-1 | 0.36+/-0.11 |
| 1:20 | 0.05+/-0.02 | | | 0.2+/-0.02 | 0.5+/-0.1 | 0.24+/-0.1 | 56+/-1 | 0.5+/-0.14 |

For all films, the pump-probe signals build up within the experimental resolution of 100 fs around zero pump-probe delay. This is due to the ultrafast formation of CT excitons in the TV38 phase and/or instantaneous splitting of the interfacial excitons in blended films [31, 80].

Transients of neat sample and 3:1 blend demonstrate a fast decay component (A_1) in sub-ns timescale (τ_1), indicating that a certain amount of photogenerated exciton and/or charges are recombined. By assumption, these recombination channels could be either

intra- or *intermolecular* recombination of CT excitons and/or charges or back electron transfer from [70]PCBM to TV38 in the BHJ samples. However, these decay components are diminishing at *high* [70]PCBM loadings and presenting in *neat* TV38 film; this allows us to rule out the possibility of back transfer from [70]PCBM to TV38. Meanwhile, similar decay component was not found in the well-separated TV38 molecules in PMMA matrix (Fig. S15) [81] where *intermolecular* interactions are negligibly low. Therefore, we can attribute this decay to *intermolecular* recombination of charges that were initially separated between neighboring molecules. Similar recombination channel was previously observed in SSM-based blends as well [23].

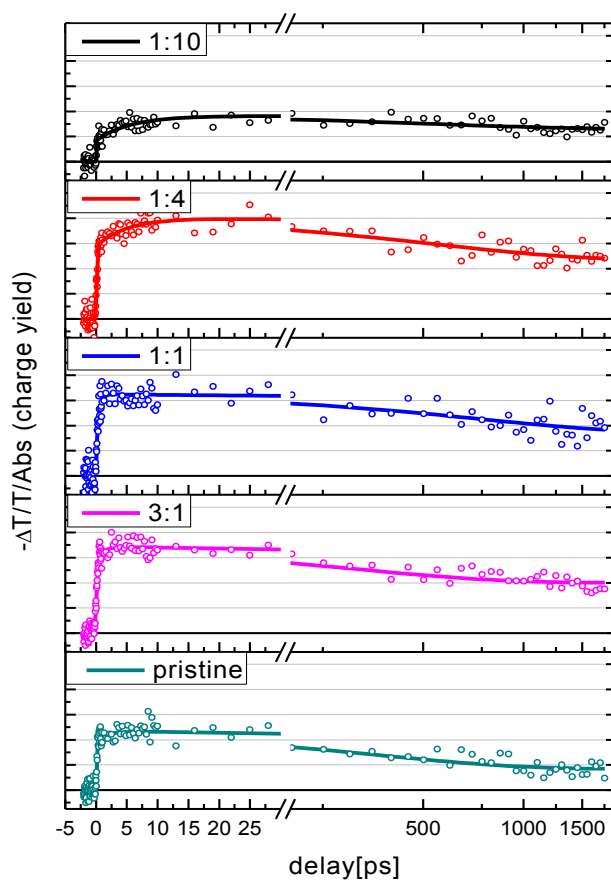


Figure 2.4 Isotropy transients for TV38:[70]PCBM blends at different [70]PCBM concentrations. Circles represent the experimental data points and solid lines stands for best fits according to Equation(1), all transients are normalized to the number of absorbed photons. Excitation and probe wavelengths were set at 520 nm and 1.3 μm , respectively

Note that the decay component (A_1) in the sub-ns time scale diminishes with the increasing concentration of [70]PCBM, i.e. the *intermolecular* recombination channel is less efficient in blends with [70]PCBM. The reason could be two fold, one is that heavier load of [70]PCBM content results in an similar effect as performed by PMMA matrix as talked above, the TV38 molecules are surrounded by [70]PCBM molecules and therefore very well

separated, which leads to a decrease of intermolecular recombination. The other reason is that a relatively large amount of generated exciton are immediately disassociated onto TV38/[70]PCBM interface after the pump pulse, thus can hardly transfer back and recombine with each other eventually. Note that the latter explanation seems to be more relevant in the blended films due to the comparable fraction of the TV38 and [70]PCBM molecules in the blend.

Another striking feature is that the initial decay is replaced by a growing component when the [70]PCBM concentration exceeds 1:1 with a time scale of ~ 2 ps for 1:1 and 1:2 blends, 6 ps for 1:4 blend and 10 ps for 1:10 blend and around 60 ps for 1:20 blend. Moreover, its amplitude and time increase with increasing concentration of [70]PCBM. From the decomposition of visible absorption it is clear that the share of [70]PCBM absorption increases with the concentration (SI 1). Therefore it is reasonable to attribute this growth to the diffusion-delayed hole-transfer process [31]. The reason is that, the excitons created on [70]PCBM have a lower probe absorption cross-section comparing to excitons and polarons on TV38. When the excitons which are initially created on [70]PCBM, diffuse to the interface and dissociate in the interfacial area, TV38 molecules are correspondingly charged, or in another word, polarons are created on TV38 molecules which leads to increasing of the signal.

To be noted is that this growing component persist to present as the [70]PCBM loads keep increasing to the ratio of 1:20, depicted in the SI 8. The fittings of the transients for high [70]PCBM load samples indicate an extending growing time, which can be an intermediate instruction of enlarged cluster size. And due to this enlarged cluster size, bulk excitons dissociations are further delayed by the diffusion.

For all blends and neat samples, decaying components at 0.5-1.2 ns timescales are observed. Interestingly, for the blended films neither timescales nor amplitudes of this component depend on the particular TV38:[70]PCBM ratio. For the neat film, this component exhibits somehow larger decay time having the same amplitude. The similar decay was also found in the sample where TV38 molecules are diluted in PMMA matrix hence there are only *intramolecular* interactions taking place (SI 5), Similar effect was observed in the SSM with TPA core and DCV acceptor groups [23]. Therefore, this effect is likely determined by extremely efficient interactions between the TPA and DCV groups, which act as a potential well for the *intramolecularly* separated charges and the charges are confined within the molecule. Charges initially separated within the same molecule recombine via this channel and do not undergo electron transfer even in blends with high concentration of [70]PCBM. Therefore, this share of separated charges does not contribute into the long lived charge proving *intramolecular* charge separation/lost channel.

However, we note that the possibilities of charge recombination via interfacial charge transfer states should not be fully ruled out. Currently, we are not able to distinguish

recombination channels like *intramolecular* channel and charge transfer state, therefore distinguishing *intramolecular* recombination and charge transfer state calls for further study.

2.4 Photoinduced Anisotropy Dynamics

To get more insights about excited state dynamics, photoinduced anisotropy transients were measured (Figure 2.5). Anisotropy experiments offer the information about evolution of orientations of photoinduced dipole moments. Note that the anisotropy signal is charge concentration or absorption cross-section independent since these two factors are reduced according to equation (3). Because the anisotropy experiment is polarization sensitive, the resulted dynamics reflect depolarization of excited state of any nature be that due to the charge migration, isotropic hole transfer process or intrinsic intramolecular depolarization of the excited state.

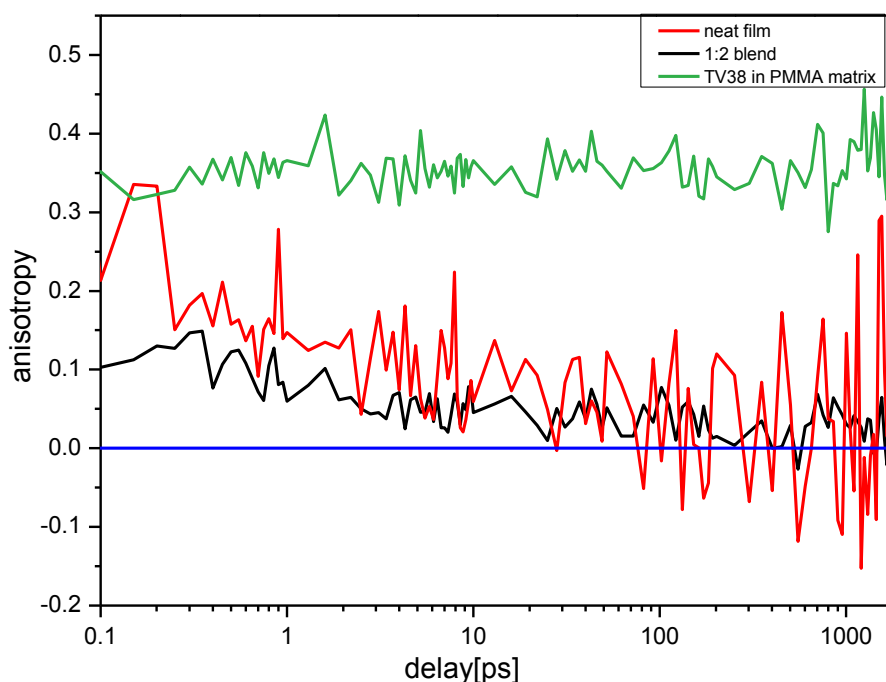


Figure 2.5 Photoinduced anisotropy of neat TV38 film (red), 1:2 film of TV38:[70]PCBM (black) and TV38 in PMMA matrix (green). Other blends have the similar dynamics with the 1:2 blend depicted here and therefore are not shown (SI 8). Excitation and probe wavelengths were set at 520 nm and 1.3 μm , respectively

In the pristine TV38 film, the initial anisotropy value is ~ 0.2 (Figure 3.3, blue line), which is twice lower as the maximal possible value of 0.4, and corresponds to the average angle of $\sim 35^\circ$ between the polarization of incoming light and the average orientation of photoinduced dipole moment (equation 5) [59]. Taking into account the linear structure of

the molecule, one can assume that the initial depolarization is due to the intermolecular separation of CT excitons. The further decay of the anisotropy within first ~ 100 ps is likely due to the exciton migration within the TV38 medium. To verify these assumptions, the anisotropy dynamics of separated TV38 molecules in PMMA matrix was measured (Figure 2.5, green line). Indeed, constant anisotropy value of ~ 0.38 was observed, which clearly points towards the *intermolecular* nature of the depolarization process. This is in sharp contrast with T2 SSM, where substantial depolarization occurs due to the ultrafast mixing of the degenerate excited states (SI 7), while the anisotropy of TV38 molecule level-off during 1.8 ns at 0.38. This leads to the conclusion of that the *intramolecular* charge transfer processes which affect the direction of polaron dipole moment due to the symmetrical structure of T2 molecule, and are absent in TV38 molecule due to the broken symmetry.

For the blended films, the anisotropy signal starts at even lower value of ~ 0.15 and decay at similar timescales. The similar decay behavior points towards the identical nature of depolarization process in neat and blended films. The lowering of initial value of anisotropy in blended films is likely due to the noticeable contribution of the isotropic hole-transfer process [31]. Overall, in all TV38-based films the anisotropy reflects *intermolecular* motion of excitons, while the *intramolecular* dynamics do not lead to the depolarization of excited state.

2.5 Efficiency of long-lived charge generation

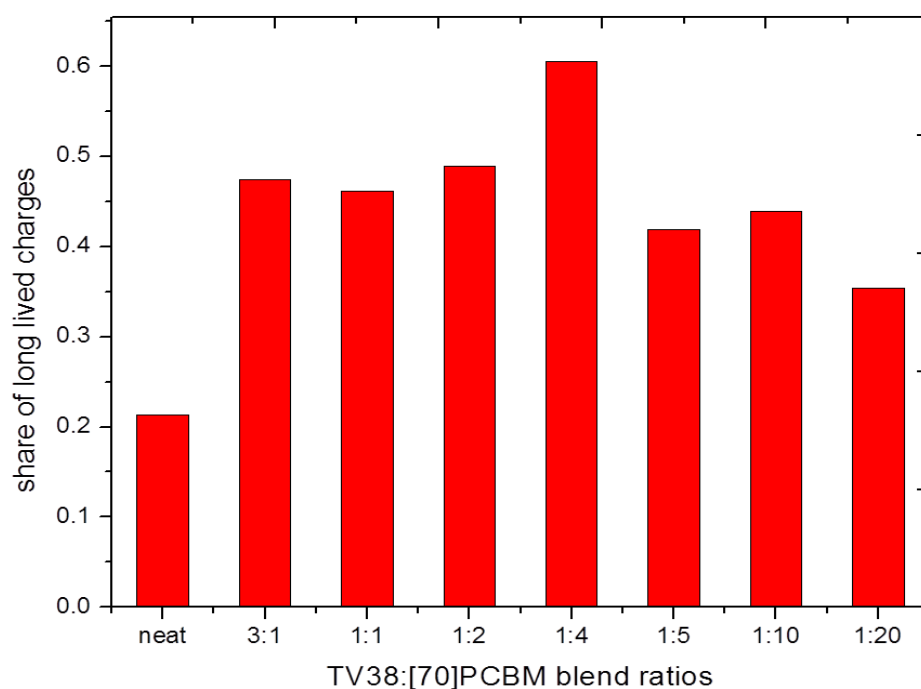


Figure 2.6 Share of the long-lived charges in TV38:[70]PCBM blends versus [70]PCBM content (red bars). Patterned areas indicate the [70]PCBM contribution to the long-lived charges via the diffusion-delayed hole transfer process.

One of the most important features of a good OSC material is the capability of providing sufficient amount of long-lived charges. The share of long lived charge in percentage of all initially generated excitons can be derived from PIA signal at long delay times.

Because all the transients were normalized to the number of absorbed photons, the amplitude of the transients are proportional to the amount of photogenerated charges per absorbed photon, with an unknown IR absorption cross-section. In order to provide the direct comparison of the relative amount of photogenerated charges, the signals were also normalized by the maximum amplitude amongst all transients, which is the transient for 1:4 sample. By this normalization, we assume that the maximal transient amplitude of 1:4 sample represents a unity polaron yield. After these normalizations, the amplitude at long delay times (>1.5 ns) straightforwardly provide the share of long-lived charges (Figure 2.6).

For the pristine TV38 film, the amount of long-lived charge is very low, hardly exceeding 20%. This is because in the neat film, no energy gradient is provided to split the CT-excitons. The photoinduced excitons have no other dissociation channels but recombine, therefore providing the least charge generation efficiency.

As [70]PCBM being added into the mixture, the share of long-lived charge increases to a relatively high level rapidly - more than 50% percent of initially separated charge survived at experimental time scale of 1.8 ns for the 1:4 TV38:[70]PCBM ratio. The reasons for tremendous increase of the long-lived charges fraction are the following. On one hand, adding of [70]PCBM acceptor opens a new pathway for charge separation: CT excitons from TV38 can be split at the interface of the BHJ due to the sufficient energy offsets for the electron transfer (Figure 2.1d). On the other hand, [70]PCBM can also absorb photons and generate excitons, therefore contributing to the long-lived charge via hole transfer process. Interestingly, the amount of long-lived charges monotonously increases with increasing of [70]PCBM concentration till 1:4. When the [70]PCBM blend ratio keeps increasing, the amplitude of long lived charge starts to decrease. With further increasing of [70]PCBM content, formation of large cluster where not all excitons can make it to the interface, it is reasonable to observe a decrease. Also, since the TV38 components in the blends are significantly reduced, insufficient HT channel can be offered by TV38 which leads to the relevant low amplitude.

The dependence of amplitude, which represents share of long lived charges, indicates that the charge generation efficiency from [70]PCBM phase is higher than from the TV38 phase, making the TV38-based OSCs essentially fullerene devices [82].

2.6 Conclusions

Charge dynamics in BHJs based on novel TV38 small molecule have been investigated with

time-resolved visible pump-IR probe ultrafast spectroscopy. It was shown, that efficient *intramolecular* recombination of TV38 CT excitons at sub-ns timescales occurs in all blends. This channel is almost independent of [70]PCBM concentration therefore hardly produces any long-lived charges. Meanwhile, in blends with low [70]PCBM content, intermolecular charge separation in TV38 phase occurs with recombination time of ~ 100 ps. However, this recombination channel seems to be fully suppressed in blends with [70]PCBM content higher than 50%, This is due to: i) larger average distance between TV38 molecules in blends with high [70]PCBM concentrations and ii) direct electron transfer from TV38 to [70]PCBM after photoexcitations. According to the relative high efficiency of the charge generation via hole transfer process, we conclude that this BHJ is a [70]PCBM based OSC system and at least 60% of initially separated charge survive over the experimental time window of 1.8ns.

In the view of device designing, 1:4 donor:acceptor ratio could be used when optimizing the BHJ architecture. However *intra*-molecular charge recombination should be suppressed to ensure high charge generation efficiency. A potential path could be to further decrease the band gap of donor material further and on the other hand increase LUMO/LUMO offset between donor and acceptor material to obtain a pronounce exciton dissociation efficiency. Another issue is the exciton diffusion distance, which also limits the charge generation efficiency. This can be optimized and overcome by morphology study with AFM technique and crystalline property study with TEM technique.

Summarizing, TPA-based SMs with oligothiophene as conjugated arm and electron accepting DCV unit offers very efficient charge generation when it is mixed with [70]PCBM acceptor . With a better optimization of blend ratio and morphology, we firmly believe inspiring increase efficiency can be achieved if the *intramolecular* recombination is suppressed.

2.7 Experimental

Sample preparation

For solution processed sample preparation, TV38 and [70]PCBM were dissolved separately in o-dichlorobenzene at a concentration of 25g/L. The solutions were stirred on a magnetic stirrer for at least 20 hours at 50 °C. The donor solution was then mixed with [70]PCBM with the volume ratios of 3:1, 1:1, 1:2, 1:4,1:5, 1:10 and 1:20. Solutions with different mixing ratios were stirred with the magnetic stirrer for at least another 2 hours. Thin films were then spin-coated (800 rpm, 2 minutes) on glass substrates. The optical densities of all films were around 0.2.

For PMMA matrix sample, PMMA was dissolved in o-dichlorobenzene at a concentration of 150 g/L. The solution was stirred on a magnetic stirrer for at least 5 hours

at 50 °C. Then the solution was mixed with o-dichlorobenzene solution of TV38 with molar concentration of 1:50, which corresponds to 1 TV38 molecule per 600000 PMMA monomers.

Optical

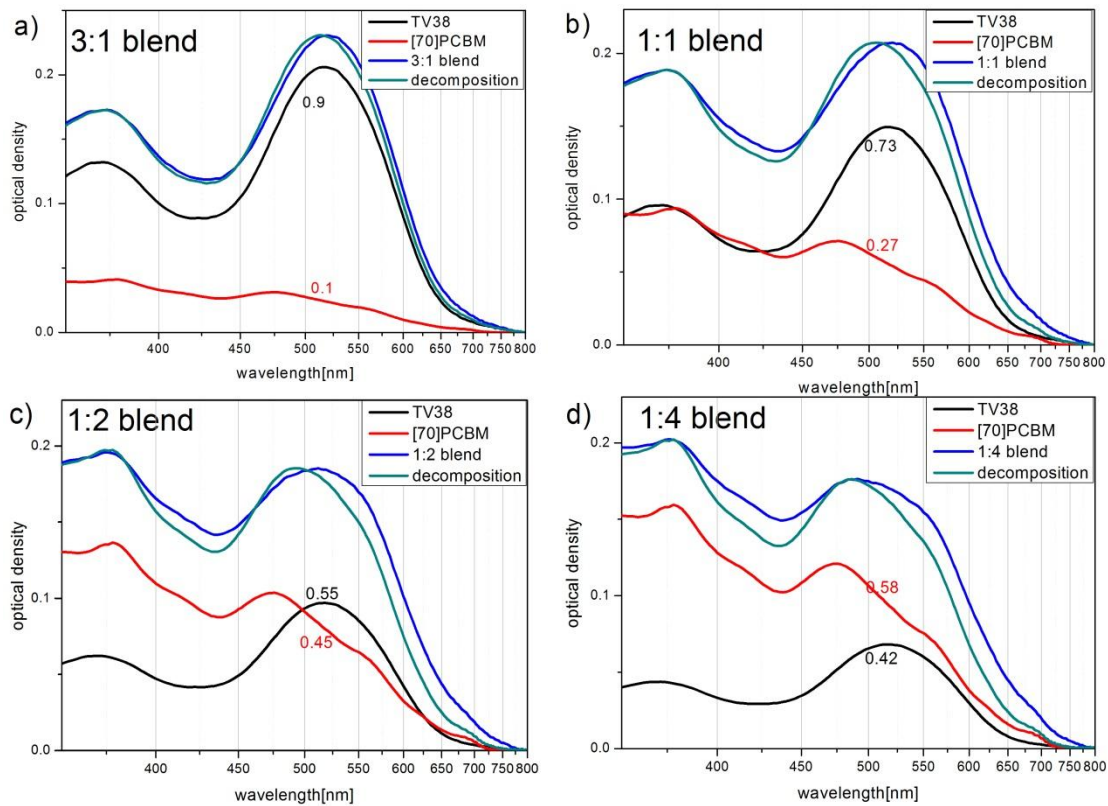
Linear absorption spectra were obtained using a PerkinElmer Lambda 900UV/VIS/NIR spectrometer. Polarization-sensitive ultrafast PIA measurements were performed on a setup based on a Ti:sapphire regenerative amplifier(Hurricane, Spectra-Physics).The output of this amplifier was used as inputs for two optical parametric amplifiers(TOPAS, Light Conversion), operating in visible (475nm to 2600nm) and infrared (1.2μm to 20 μm) regions. The outputs of these amplifiers were utilized as pump and probe beams respectively.

The polarization of the infra-red probe beam was in an angle of 45° with respect to the polarization of the pump beam. After the sample, the parallel and perpendicular components of the probe beam (denoted as $T_{//}$ and T_{\perp}) were selected by two wire-grid polarizers, and then detected by two nitrogen-cooled InSb photodiode detectors. The isotropy population signal and photoinduced anisotropy were calculated according to equations (2) and (3).

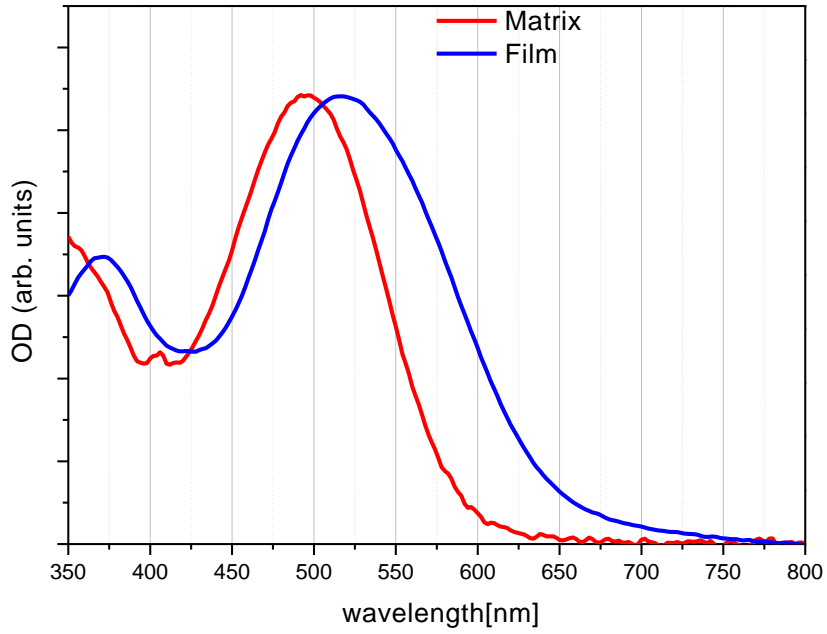
The average angle between the polarization of incoming light and photoinduced dipole moment was calculated by the following expression, in which α represents the average angle and r_0 is maximal possible anisotropy of 0.4:

$$r = r_0(1 - \frac{3}{2}\sin^2(\alpha)) \quad (5)$$

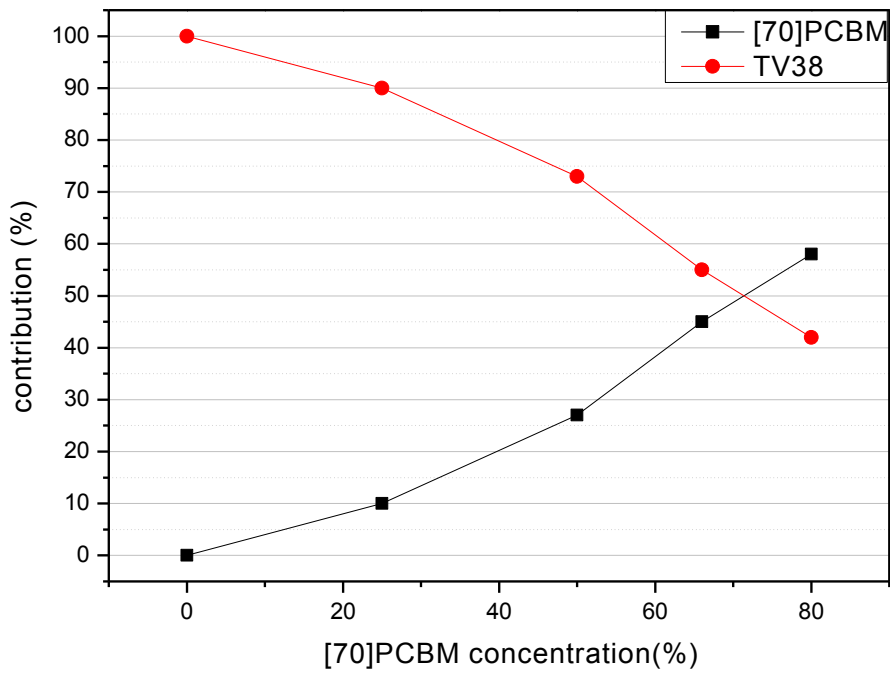
2.8 Supplementary Information



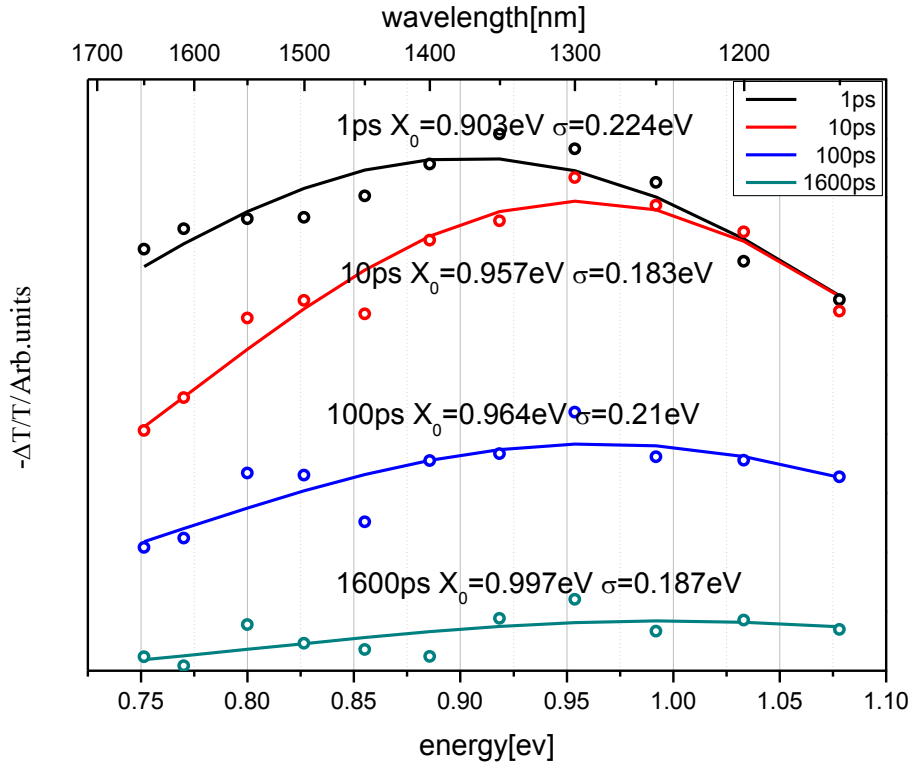
SI 1 Absorption spectra of TV38:[70]PCBM blends for different concentration (blue), and their decomposition (cyan) as sums of the TV38 (black) and [70]PCBM (red) absorption spectra. The black and red numbers represent shares in absorption of the TV38 and fullerene respectively at the excitation wavelength of 519nm.



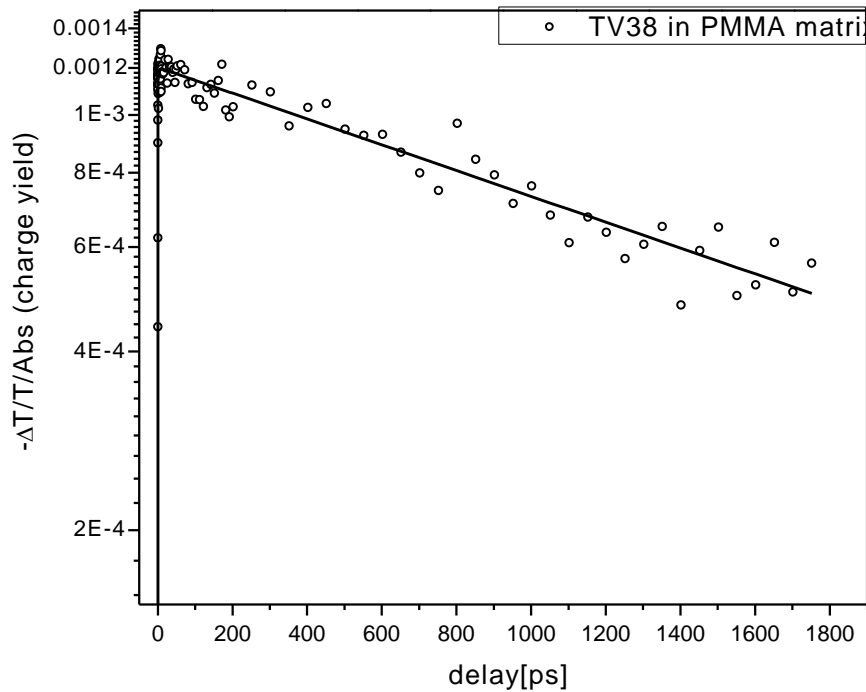
SI 2 Normalized absorption of TV38 molecules in PMMA matrix (red) and TV38 spin-casted film (blue). Clear red-shift of the absorption peak is observed in the film due to the intermolecular interactions.



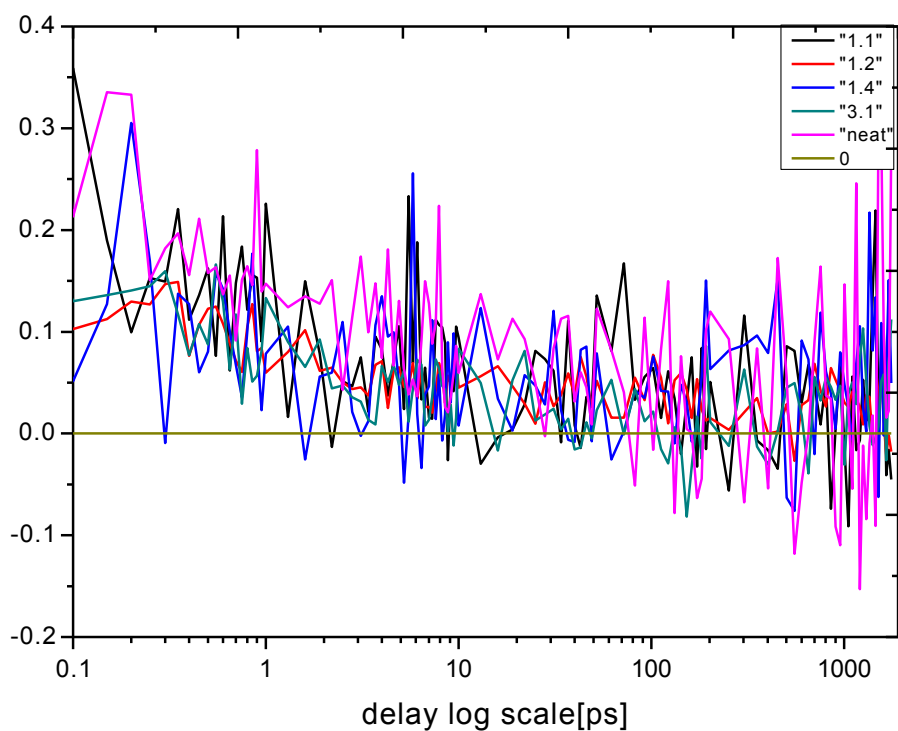
SI 3 TV38 (red) and [70]PCBM (black) contributions to the overall blend absorption at the excitation wavelength of 519nm.



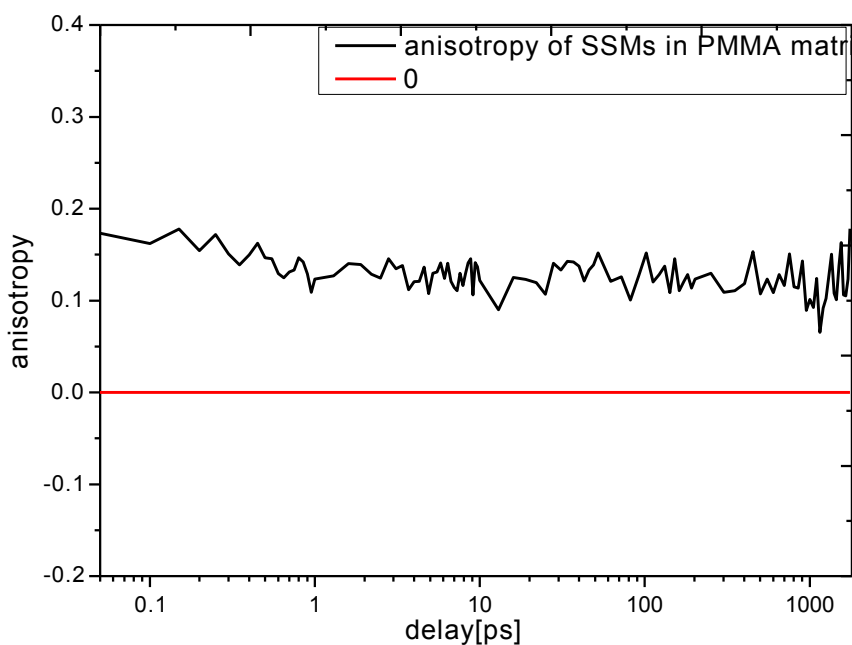
SI 4 IR PIA spectra of pristine TV38 film at different delays, open circles represent experimental data, solid lines are the fitting of experimental data with Gaussian functions. Fitting parameters are labeled beside the curves.



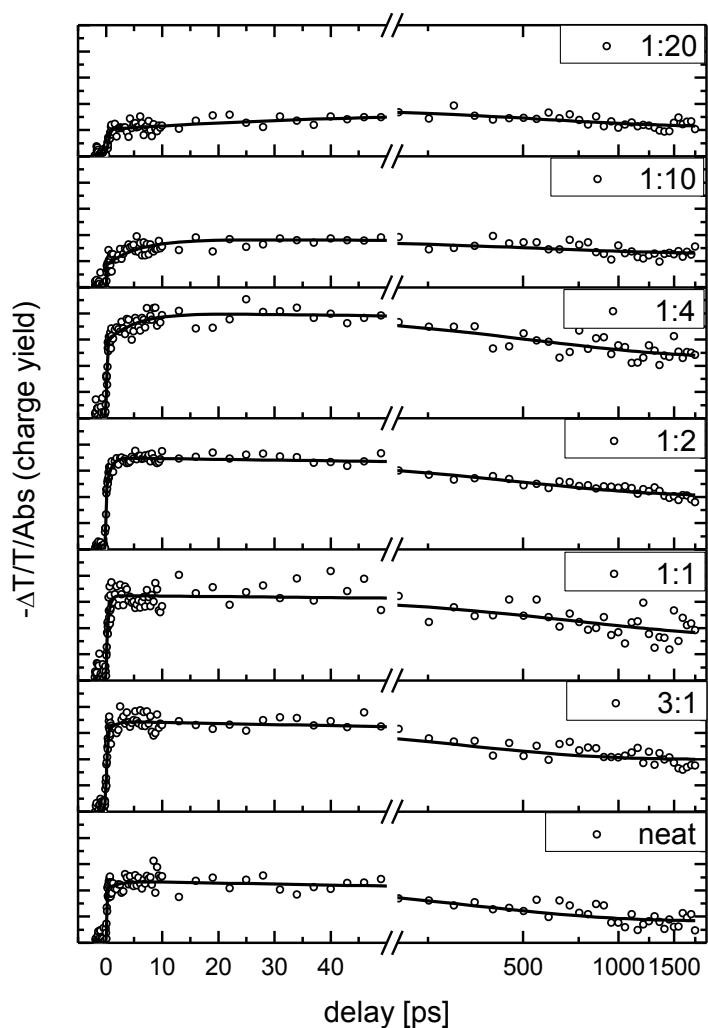
SI 5 Isotropy PIA transient of TV38 molecule in PMMA matrix. Symbols represent experimental data, while solid line represents the monoexponential fit with decay time of 1.8 ns. Excitation and probe wavelengths were set at 520 nm and 1.3 μm , respectively



SI 6 Anisotropy of all films. All blends have almost the same decay behaviors except for the neat film. Excitation and probe wavelengths were set at 520 nm and 1.3 μm , respectively



SI 7 Anisotropy of SSM T2 in PMMA matrix. A decay occurs in a sub-ps time scale indicates the ultrafast intramolecular charge redistribution. On a longer time scale, a constant anisotropy can be observed, indicating the absence of intermolecular charge transfer or exciton migration. Excitation and probe wavelengths were set at 520 nm and 1.3 μm , respectively



SI 8 Isotropy transients for TV38:[70]PCBM blends at different [70]PCBM concentrations. Circles represent the experimental data points and solid lines stands for best fits according to Equation(1), all transients are normalized to the number of absorbed photons. Notice a persist growing component as the [70]PCBM ratio is increasing at the initial stage. Excitation and probe wavelengths were set at 520 nm and 1.3 μm , respectively

3. Chapter 3: Exciton diffusion in vacuum-deposited TV38 heterojunction

3.1 Introduction

In the active layer of organic solar cells (OSCs), after light absorption Frenkel excitons are created which cannot be split only by the thermal energy of the system due to their relatively high binding energy of ~ 0.3 eV [50, 83]. Therefore, a donor-acceptor type interface between two materials is required to provide the driving energy for splitting the exciton into charges. A simplest type of the interface is the bilayer of donor- and acceptor-type materials [42]. Since the Frenkel excitons in organic materials demonstrate rather limited diffusion length [34], there is always a compromise between film thickness (which determines the efficiency of photon absorption) and the exciton diffusion length. If the film has too small thickness as compared to the exciton diffusion length, the exciton harvesting efficiency is high but the photon-to-exciton harvesting is low. On the other extreme, if the layer thickness exceeds the light penetration depth, the majority of photons are collected but a large share of excitons dies within the exciton lifetime before having made it to the interface. To solve this dilemma, Yu *et. al.* came up with the idea of bulk-heterojunction (BHJ) concept in 1995 [22].

BHJ is a nanoscaled mixture of donor-type and acceptor-type materials. In the BHJ, the materials form a fine structure with typical dimensions smaller than the exciton diffusion length (~ 10 nm [10, 84]), and therefore the active layer thickness can be substantially increased without losses in exciton harvesting. Well-designed BHJ can achieve a near unity efficiency of exciton dissociation [10]. Unfortunately, it is hard to quantitatively control and optimize BHJ's morphology, molecular packing, phase separation and purity etc. which all have a significant impact on the photon-to-voltage conversion efficiency. Therefore, optimizing the BHJ is a laborious work based on the trial-and-error approach. This is in sharp contrast with simple well-defined bilayer heterostructure, which can be vacuum-deposited in a highly controllable way with predefined parameters. Therefore, an alternative to BHJ approach to maximize the photon harvesting is to design new materials where the exciton diffusion length and the light penetration depth are well-balanced.

Among the acceptor materials, C_{70} fullerene combine both high absorption coefficient [68] and long exciton diffusion lengths [36, 85, 86]. However, the lack of simple and efficient donor materials prevented manufacturing of high-efficient vacuum-deposited OSCs. TV38 small molecule is suitable for vacuum deposition and demonstrates good

absorption properties, so that it can be considered as a suitable candidate for donor materials in bilayer OSC.

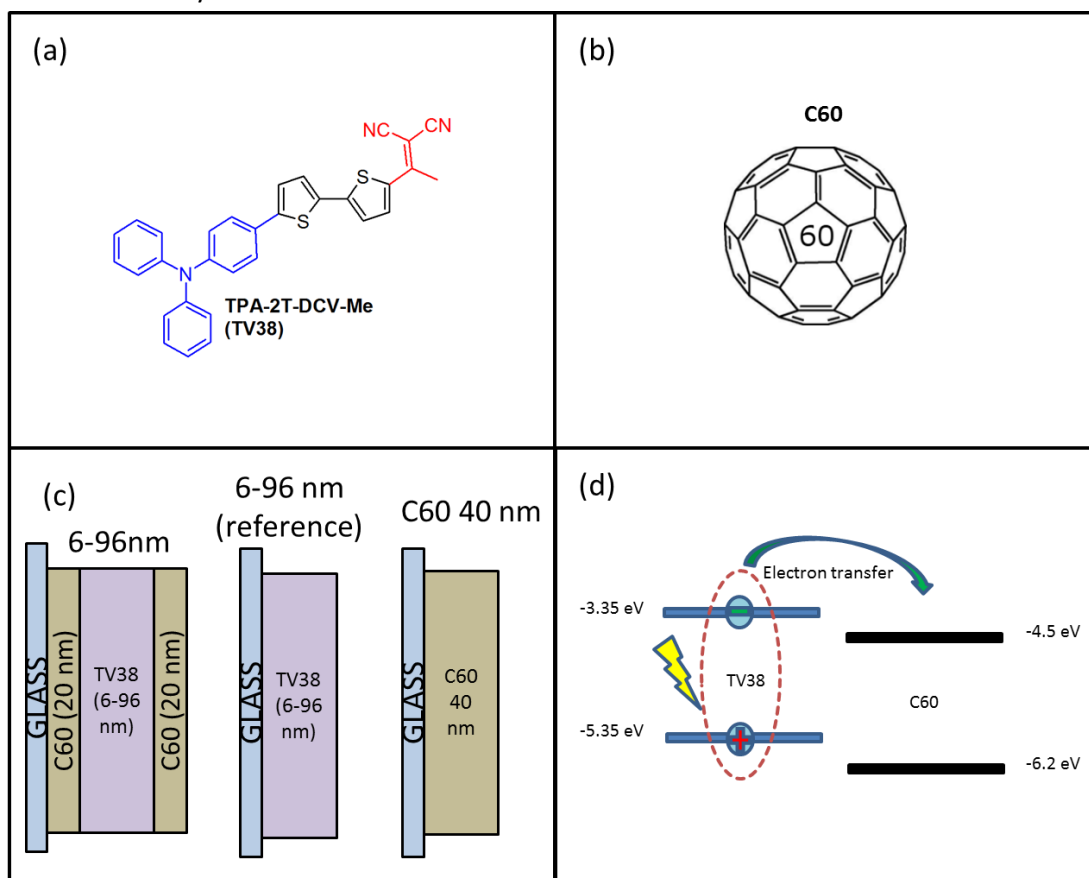


Figure 3.1 Chemical structures of TV38 electron donor (a) and C_{60} electron acceptor (b). (c) Structure of vacuum-deposited multilayered structures with 6-96 nm TV38 layers and 20 nm C_{60} quencher, vacuum-deposited 6-96 nm TV38 layers and 40 nm C_{60} layer are used as reference samples. (d) Frontier energy levels of TV38 and C_{60} . The process of electron transfer is depicted by an arrow.

In this Chapter, we investigate the exciton diffusion in TV38 layers with time-resolved photoinduced absorption (PIA) spectroscopy. The main focus is to obtain the exciton diffusion distance in vacuum-deposited layers based on TV38 molecule and to compare it with the light penetration depth. Diffusion dynamics were tracked by time-resolved PIA technique and analyzed with a simple analytical model of exciton diffusion in continuous medium. The exciton diffusion length in the vacuum-deposited TV38 layers is estimated to be around 10 nm, which is significantly shorter than the light penetration depth of around 80 nm. The analytical model perfectly describes the exciton diffusion in thick (96 nm and 48 nm) and thin (6 nm) TV 38 layers, but fails in describing exciton dynamics in 12 nm and 24 nm samples. We attribute this discrepancy to the complex interplay between exciton and polaron dynamics, which are most probably driven by formation of the surface charge transfer states and/or exciton trapping in the TV38 layer.

Therefore, the optimization of molecular packing and surface morphology is envisioned to be a perspective way to increase the crystallinity of TV38 and the exciton diffusion length.

3.2. Absorption Spectra

3.2.1 UV-VIS absorption

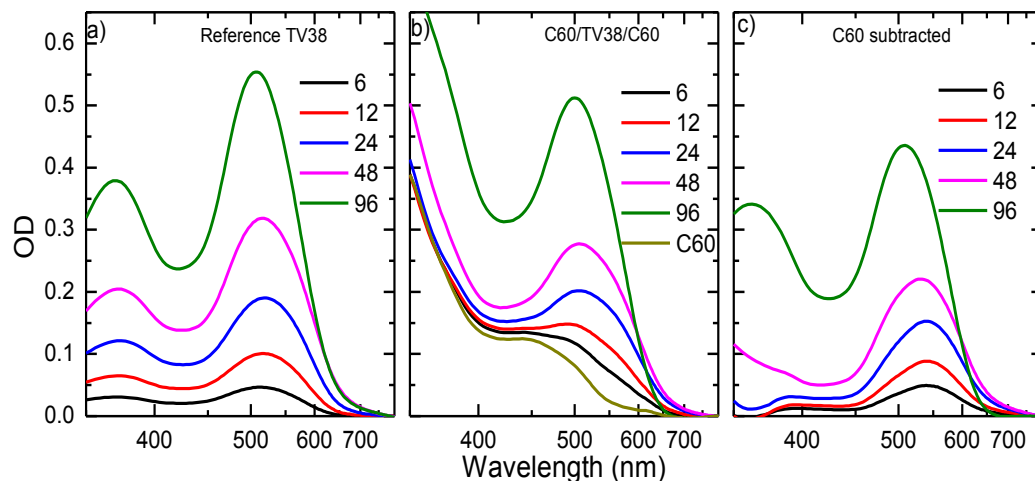


Figure 3.2 Absorption spectra of the reference TV38 (a), sandwiched C_{60} /TV38/ C_{60} (b) and C_{60} /TV38/ C_{60} samples with subtracted C_{60} absorption (c). Absorption of a 40 nm C_{60} layer is also shown in (b).

Absorption spectra of the layered samples are shown in Figure 3.2. Neat TV38 samples demonstrate two strong and broad absorption peaks in the visible region, located at around 380 nm and 510 nm. The origin of these spectral features was discussed in the previous chapter (see chapter 2); both peaks have mainly the charge transfer origin. The low-energy absorption band centered at 510 nm is blue-shifted for the layered samples comparing to the solution processed ones (520 nm). We assume that the reason is different interactions between neighboring molecules in solution processed samples and in the vacuum-evaporated samples due to the different molecular packing. Most probably, vacuum-deposited films are more ordered compared to solution processed films which leads to the blue-shift of the absorption.

The C_{60} layers have a strong absorption below 400 nm, and minor absorption above 550 nm. The sharp contrast in absorption between TV38 and C_{60} in the region above 550 nm provides a good opportunity to conduct PIA experiments in such a way that mainly the TV38 molecules are excited. Therefore, the excitons are mainly planted in the TV38 layer while the direct excitation of C_{60} is largely avoided. To achieve both high optical contrast between TV38 and C_{60} and sufficient TV38 response, in the later-described PIA experiments

the pump wavelength was set at 560 nm.

Surprisingly, for the reference samples, absorption peak positions depend on the layer thickness: a minor but yet noticeable *red*-shift of the 510 nm peak is observed. The peak shifts from 510 nm for 96 nm TV38 layer to 520 nm for 24 nm layer. One of the possible explanations could be interference effects in the thin TV38 layer [36]. To investigate these shifts, the transmissions of all reference samples were measured in such a way that the polarized incident light was set under the Brewster angle with respect to the film surface, thus reflections at the interfaces were largely eliminated. The laser wavelength was close to the absorption maximum of TV38 (532 nm). The power of incident, transmitted and reflected light was measured for each sample, and the optical densities were recalculated. The results are shown in Figure 3.3. Indeed, some difference between the transmissions measured by spectrometer and laser measurements are observed with 12 nm, 24 nm, 48 nm samples. The absorbance of the sample measured with the laser scales perfectly linearly with the TV38 layer thickness, while the absorption measured with the spectrometer is somehow nonlinear. This behavior clearly points to the sensitivity of the spectrometer to interference effects.

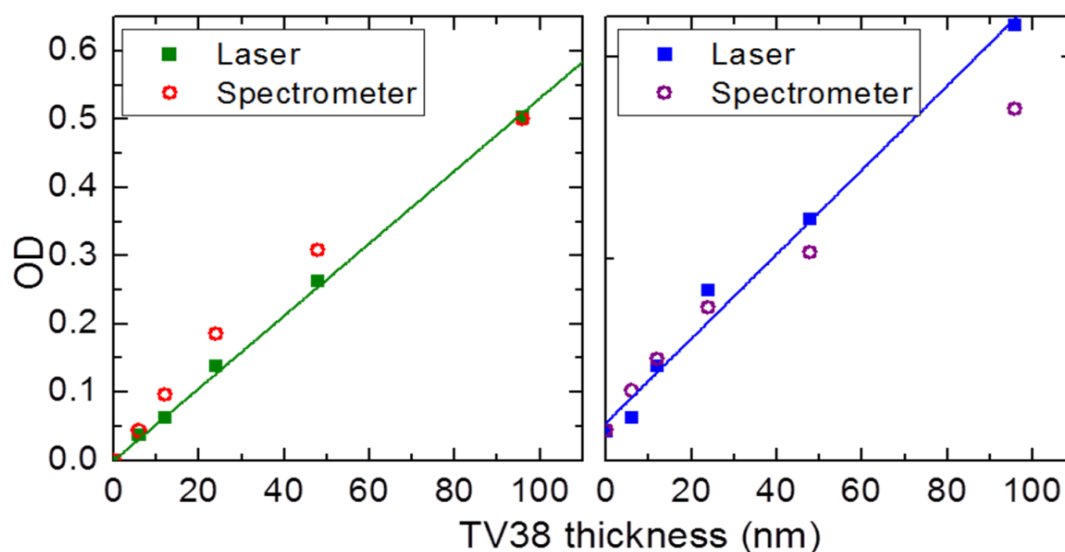


Figure 3.3 Optical densities of the reference samples and the samples sandwiched between C_{60} layers, red and purple open circles are optical densities measured by spectrometer, green and blue solid squares are optical densities measured by laser set under the Brewster angle. Green and blue lines are the best fit of laser measurements.

In the layered samples with C_{60} , the absorption peaks of TV38 are heavily affected by C_{60} absorption. As shown in Figure 3.2(b), the 510 nm absorption peak of the samples with C_{60} is observed to be *blue*-shifted from 510 nm for 96 nm sample to 460 nm for 6 nm sample, due to the increased share of C_{60} absorption, which has a *blue*-shifted peak at ~ 450 nm (figure 2(b), yellow curve). In order to isolate the TV38 absorption, a direct subtraction

of C_{60} absorption from the absorption spectra was performed; the results are shown in Figure 3.2(c). Since C_{60} layer is identical in all samples, the spectral shape should remain unchanged after C_{60} subtraction, with only variations in absorption amplitude due to different thicknesses of the TV38 layer. However, this is not the case as a noticeable *red-shift* on the TV38's green peak is observed in the absorption spectra of the layered samples. The peak at 510 nm for 96 nm sample is red-shifted to 545 nm for 12 nm and 6 nm samples (Figure 3.3a). Note the red shift levels-off at the wavelength of 545 nm. We assume that this shift is most probably caused by the interference as already mentioned above.

Therefore, we performed the same Brewster angle laser measurements as mentioned above. A clear disagreement was shown by the data measured by spectrometer and laser (which was set under the Brewster angle) respectively. As the thickness increases, the destructive interference impact increases and in turn leads to reduce of absorption at this wavelength. Note that the fitted line (green and blue) of Brewster's angle laser measurements for samples sandwiched with C_{60} and reference samples have identical slopes, while the data measured by spectrometer are quite different for sandwiched samples and reference samples. This is indicative of the strong interference effect.

However, interactions between TV38 molecules and C_{60} molecules, i.e. by formation of the interfacial CT states [78] should not be fully eliminated. That is because of the appearance of the red shoulder exists and locating around 700 nm, where neither of the materials absorbs Figure 3.2 a and b. It can be both because of extremely efficient constructive interference in this region or due to the CT state formation. Note, however, that the influence of CT states in linear sample should be much lower compared to the BHJ samples due to the lower surface area.

For an organic solar cell material, it is important that the exciton diffusion length is comparable to the light penetration depth to achieve the maximum exciton collection efficiency. From Figure 3.3, the optical density of 96 nm sample at pump wavelength is obtained as 0.55, which corresponds to 70% absorption. Therefore, we estimate the penetration depth (which corresponds to transmission of $e^{-1}=0.37$) to be around 80 nm.

3.2.2 Photoinduced infrared absorption

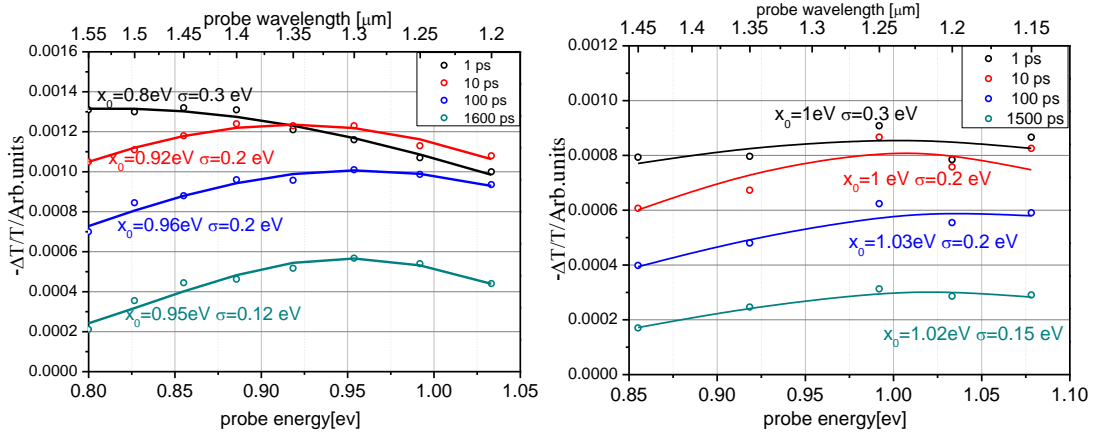


Figure 3.4 PIA spectra of 96 nm sample and 24 nm sample with the C_{60} layer. Open symbols are experimental data, solid lines are the fits of experimental data with Gaussian functions. Fitting parameters are indicated next to the curves. Excitation and probe wavelengths were set at 520 nm and 1.3 μm , respectively

Figure 3.4 shows the PIA spectra for 96 nm and 24 nm samples sandwiched between C_{60} layers. The spectra are reconstructed from the PIA transients that were measured at different probe wavelengths. Within the first 1 ps, the PIA signal is solely from the response of excitons since the share of excitons generated at the interface (which dissociate instantaneously) is negligibly low. At the longer time scale, the excitons diffuse to the interface and split into charges. Therefore, the PIA response signal consists of two parts, which are the exciton response (i.e. response of CT excitons in TV38 phase) and the low-energy polaron response (i.e. response of separated charges). However, due to unknown IR probe absorption cross sections the exciton and polaron responses cannot be distinguished straightforwardly.

Previously, with the solution processed samples, the low-energy polaron absorption band was measured to be located around 0.96 eV (see chapter 2). For the vacuum-evaporated sample, this polaron absorption band is expected to be around the same energy of 0.96 eV since the chemical structure of TV38 should not be changed by the evaporation process.

Indeed, as can be seen from Figure 3.4(a), for the sample of 96 nm sandwiched between the C_{60} layers, the CT exciton absorption peaks stabilized at ~ 0.95 eV after a 0.1 eV. A *blue-shift* has occurred within the initial 10 ps. Note that similar *blue-shift* was also observed in the solution-processed sample, pointing towards similar origin of the response, which we have previously explained as caused by the transient environment polarisability. Moreover, noticeable narrowing of the spectrum observed at large delays, which most probably points to polaron-dominated response at long timescales.

For the 24 nm thick sample with C_{60} layers, the whole spectrum is blue shifted to ~ 1 eV. This difference is most probably caused by the different molecular packing due to different sample thickness. In vacuum-deposited films, the molecules are expected to be packed with a higher order than that in the solution processed films. It is known that polaron absorption can be affected by the film packing [87], therefore some differences between solution-processed and vacuum-deposited layers of different thicknesses are expected. However the probability of the different interplay between excitons and polarons should not be fully eliminated.

To track the dynamics of exciton separation, a single probe wavelength was chosen close to the maximum of unaffected CT-exciton spectrum at 1.3 μm .

3.3 Photoinduced Absorption Dynamics

Figure 3.5(a) shows the PIA isotropy transients of the TV38 reference samples with different layer thicknesses. The transients are normalized to their maxima. Since the amplitude of PIA signal is proportional to the concentration of charges/CT excitons, by normalization to maxima we assume near time zero, initially generated excitons have the same density in different samples.

With the reference sample we assume that the PIA response is solely given by CT excitons since there is no acceptor material thus excitons will not be quenched. Hence the decay is assigned to the exciton recombination. Therefore, the dynamics for different samples are expected to be similar, which is not the case. The signal behavior has a dependence on the layer thickness, which is that the decay appeared to be faster for thinner samples. This is most probably due to the exciton quenching at the TV38/air and/or TV38/glass interfaces in the thinner samples.

Figure 3.5(b) shows exciton dissociation dynamics for the C_{60} sandwiched samples. For the thick samples (24 nm – 96 nm) the early-time dynamics are still dominated by the exciton response due to low share of excitons generated in close proximity to the interface, while for thinner samples the initial signal may consist both of exciton and polaron responses. The signals at long delays (>1.5 ns) for all samples consist of both exciton and polaron responses with unknown ratio. To make sure that the C_{60} response does not affect the transients, we measured the PIA signal from a 40 nm C_{60} layer which was at least a factor of 15 lower than the exciton response for 96 nm sample.

Since for all samples prominent decay of the signal is observed, even though for thin samples the exciton harvesting efficiency is expected to be high, it is reasonable to assume that IR cross-section of CT excitons is much larger compared to that of polarons. To estimate the relative polaron cross-section, we assume 100% exciton harvesting efficiency in the thinnest 6 nm sample. In this case at time zero the response is originated mainly

from the CT excitons. At long delays, majority of the excitons should be able to diffuse to the interface and thus are split there. Hence the signal is produced only by the separated charges, i.e. the PIA response has a polaron origin in this case.

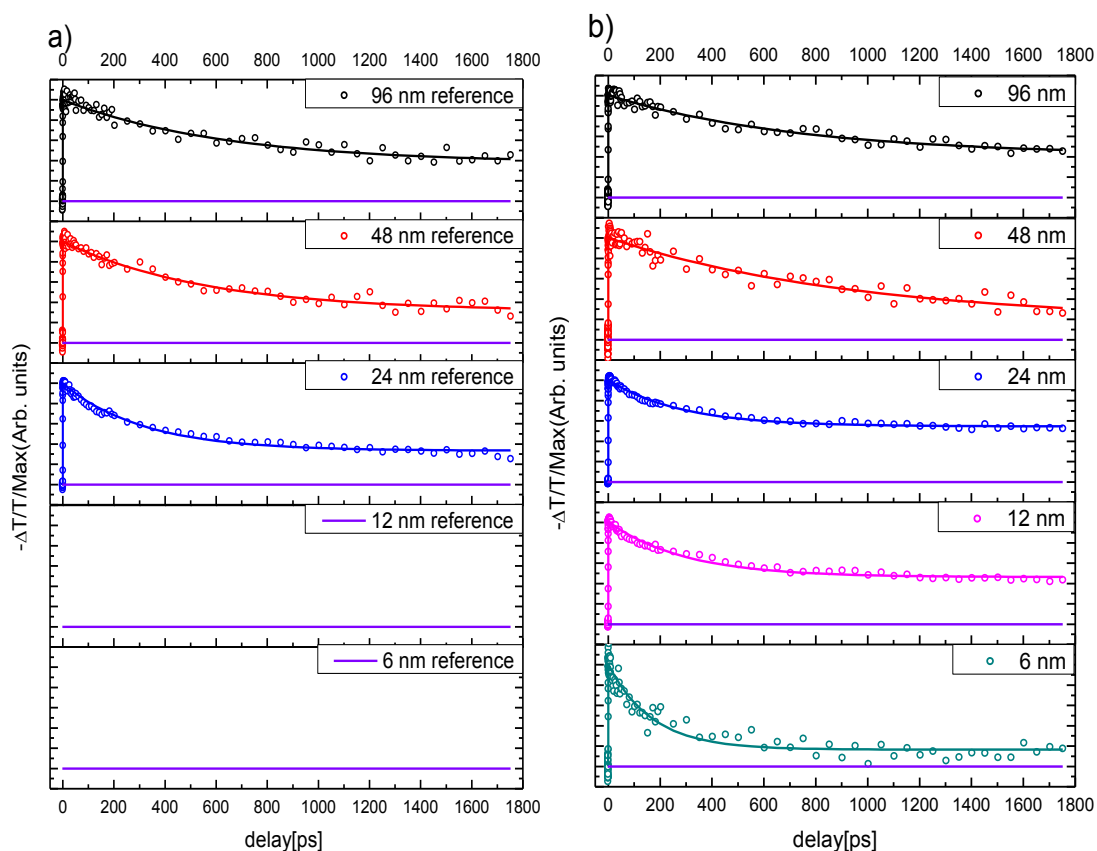


Figure 3.5 Isotropy transients for reference TV38 samples (a) and $C_{60}/TV38/C_{60}$ samples (b) with different layer thickness. Circles represent the experimental data points and solid lines show the fits according to a multi-exponential decay function with a baseline. Note that the fits are only for guiding the eyes and their parameters cannot be used as a description of the real charge transfer process. All transients are normalized to the maxima near zero pump-probe delay. 12 nm and 6 nm reference samples were not measured because of extremely weak signals. Purple lines represent $Y=0$ for each transient. Excitation and probe wavelengths were set at 520 nm and 1.3 μm , respectively

As can be seen in Figure 3.5(b), the PIA signal at long delay for 6 nm sample is ~ 0.2 . This allowed us to estimate the relative absorption cross-section of charges as only 20% of the CT exciton absorption cross-section. Therefore, we can conclude that the initial accelerations of the PIA dynamics in sandwiched samples are due to the exciton quenching at the interfaces. In the previous chapter, similar exciton and polaron absorption cross-section were assumed, which is likely not the case here. This difference is most probably caused by the different molecular packing because of different process methods [87] as mentioned above. Note that for the 6 nm sample C_{60} absorption cannot be fully

neglected (Figure 3.2b), therefore C_{60} excitons could dissociate into the separated charges and contribute to the charges, thus the polaron cross-section could be slightly overestimated.

Since the exciton cross-section is much larger than the polaron cross-section and the exciton lifetime is fairly long (~ 2 ns, Figure 3.5a), one would expect monotonous increase of the long-delay signal amplitude with layer thickness due to the higher contribution of CT excitons. However, at the longer time scale the transient amplitudes are not in line with this assumption.

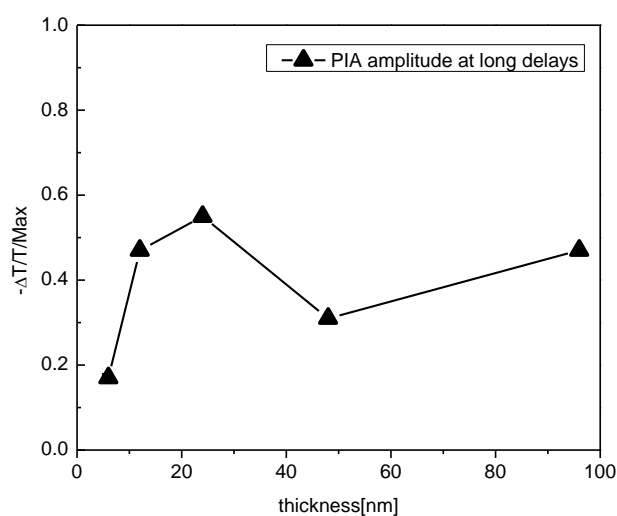


Figure 3.6. PIA amplitudes at 1500-1800 ps delays for the sandwiched samples.. Note strong nonlinearity of the PIA signal dependence on the TV38 layer thickness.

As shown in Figure 3.6, the long-time amplitude firstly increases rapidly for 12 nm and 24 nm samples. This can be understood as the share of exciton response with higher cross-section increases with the thickness. However, when the thickness reaches 48 nm, the amplitude decreases tremendously. For the 96 nm samples the amplitude increases back as expected due to the increased share of CT excitons. The unusual growth in amplitudes for 12 nm and 24 nm sample at the long-time tail of the transients points towards complex processes of exciton separation and recombination. For example, if immobile excitons are generated within the TV38 layer (see Chapter 2), they can contribute to the CT exciton response but not contribute to the diffusion process, making the dynamics complicated. The exciton delocalization can also affect the PIA dynamics in a complex way.

3.4 Analytical model

To quantitatively describe the results, an analytical model was developed. The model is based on the diffusion of localized excitons with the finite lifetime in a medium sandwiched between two quenching layers. The schematics of the processes are depicted in Figure 3.7.

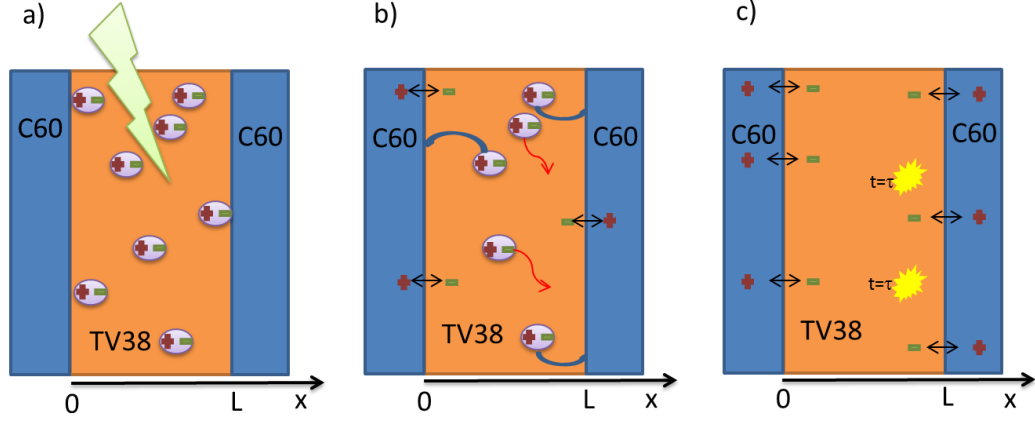


Figure 3.7 Schematic illustration of the exciton generation, diffusion, dissociation processes, L is the layer thickness; x is the spatial coordinate. a) The exciton generation. b) The instant splitting of the interfacial excitons and bulk exciton diffusion to the interface (indicated by arrows), c) The dissociation of all excitons and recombination of bulk exciton (marked by the red arrows in b) with the lifetime of τ .

Since the dynamics of exciton concentration and distribution are time and space evolutionary processes [32], to describe the dynamics, we employed the following continuity equation [36, 88, 89]:

$$\frac{\partial n(x,t)}{\partial t} = -\frac{n(x,t)}{\tau} + D \frac{\partial^2 n(x,t)}{\partial x^2} - S(x)n(x,t) + G(x,t) \quad (6)$$

Here n is the concentration of excitons, x is a spatial coordinate along the light propagation direction, τ represents the effective exciton life time and D is the diffusion coefficient of the excitons. The first term in the right-hand side of Eq.6 describes the decay of excitons via radioactive and non-radioactive recombine processes, with a constant decay time τ . The second term describes the exciton diffusion with the diffusion coefficient D .

The third term stands for the exciton separation processes at the interface. We assume 100% harvesting efficiency at the interfaces since the C_{60} layers work as a very good exciton quencher [33, 90], which basically means that all the excitons diffused to the interface split into charges. In the equation, we describe this in the third term with the boundary conditions (assuming the $C_{60}/TV38$ interface to be located at $x=0$ and $x=L$, where L is the thickness of the TV38 layer):

$$n(L,t) = n(0,t) = 0 \quad (7)$$

The fourth term is an exciton generation term $G(x, t)$. For simplicity we assume a uniform initial distribution of excitons. Therefore the term $G(x, t)$ can be replaced by the initial conditions:

$$n(x, 0) = N_0 \quad (8)$$

Therefore, equation (1) is simplified to the following equations with initial and boundary conditions:

$$\begin{cases} \frac{\partial n(x, t)}{\partial t} = -\frac{n(x, t)}{\tau} + D \frac{\partial^2 n(x, t)}{\partial x^2} & (9) \\ n(x, 0) = N_0 & (10) \\ n(L, t) = n(0, t) = 0 & (11) \end{cases}$$

The solution was sought in a form: $n(x, t) = T(t)X(x)$. By separating the variables:

$$\begin{cases} T(t) = e^{-\frac{t}{\tau}} e^{-t\lambda^2} & (12) \\ Z(z) = A \cos(\omega z) + B \sin(\omega z) & (13) \end{cases}$$

where $\omega = \sqrt{\lambda^2/D}$. By applying the boundary conditions:

$$\begin{cases} A = 0 & (14) \\ \omega_k = \frac{\pi k}{L} & (15) \end{cases}$$

Therefore, the bulk exciton density is

$$n(z, t) = e^{-t/\tau} \sum_{k=1}^{\infty} B_k e^{-\omega_k^2 D t} \sin(\omega_k x) \quad (16)$$

and

$$B_k = \frac{2}{L} \int_0^L N_0 \sin(\omega_k x) dx \quad (17)$$

Therefore the exciton density in a film with quenching material attached on both sides can be derived as:

$$n(x, t) = \frac{4N_0}{L} e^{-t/\tau} \sum_{i=1}^{\infty} \frac{e^{-\omega_{2i-1}^2 D t}}{\omega_{2i-1}^2} \sin \omega_{2i-1} x \quad (18)$$

At the both interfaces, the excitons dissociate into charges. This process can be considered as a flux of excitons through boundaries, which can be determined with the boundary condition as following [36]:

$$J(t)|_{z=0,L} = \pm D \frac{dn(z,t)}{dz} \Big|_{z=0,L} \quad (19)$$

Therefore the concentration of polarons in the TV38 layer by a delay time t is the time integration of the flux:

$$h(t) = - \int_0^t \left(D \frac{dn(x,t)}{dx} \Big|_{x=0} - D \frac{dn(x,t)}{dx} \Big|_{x=L} \right) dt \quad (20)$$

The PIA response of bulk exciton and polarons are proportional to the integral of exciton density and hole density over the layer thickness L . The responses are shown in the following expressions:

$$\left\{ \begin{aligned} N_{eb}(t) &= \frac{8}{L^2} e^{-t/\tau} \sum_{i=1}^{\infty} \frac{e^{-\omega_{2i-1}^2 D t}}{\omega_{2i-1}^2} \end{aligned} \right. \quad (21)$$

$$\left\{ \begin{aligned} N_{hb}(t) &= \frac{8D}{L^2} \sum_{k=1}^{\infty} \frac{1 - e^{-t(\frac{1}{\tau} + \omega_{2k-1}^2 D)}}{1 + \omega_{2k-1}^2 D \tau} \tau \end{aligned} \right. \quad (22)$$

Note that Equations (21)-(22) describe exciton diffusion in continuous medium, where the contribution of interfacial excitons (which dissociate without any diffusion process) is negligible. This is indeed true for thick (>48 nm) samples. However, for thinner samples the interfacial excitons noticeably contribute to the signal and should be taken into account. Therefore, we add the interfacial component to equations (23)-(24) to acquire the real exciton and hole response, which has a dissociation time within electron-transfer time scale T_{et} , since no precluding diffusion is required [36]. The bulk part and interfacial part are connected with a share ratio of γ which is calculated as $2/L$, where L is the sample thickness (assuming the excitons are localized). The whole response of excitons and holes is expressed as:

$$\left\{ \begin{aligned} E(t) &= \gamma e^{-\frac{t}{T_{et}}} \cdot N_{eb}(0) + N_{eb}(t) \end{aligned} \right. \quad (23)$$

$$\left\{ \begin{aligned} H(t) &= \gamma \left(1 - e^{-\frac{t}{T_{ht}}}\right) \cdot N_{eb}(0) + N_{hb}(t) \end{aligned} \right. \quad (24)$$

Finally, we assume the exciton absorption cross-section of unity and the polaron absorption cross-section of σ , put all calculated terms in the following expression

$$S(t) = \sigma H(t) + E(t) \quad (25)$$

and fit the experimental data with this equation. The results are shown in Figure 3.8. In the fitting function, T_{et} was fixed at 0.1 ps [31, 80] and σ was equal 0.2 (see above), while exciton diffusion coefficient D and exciton lifetime τ were fitted globally for all the transients.

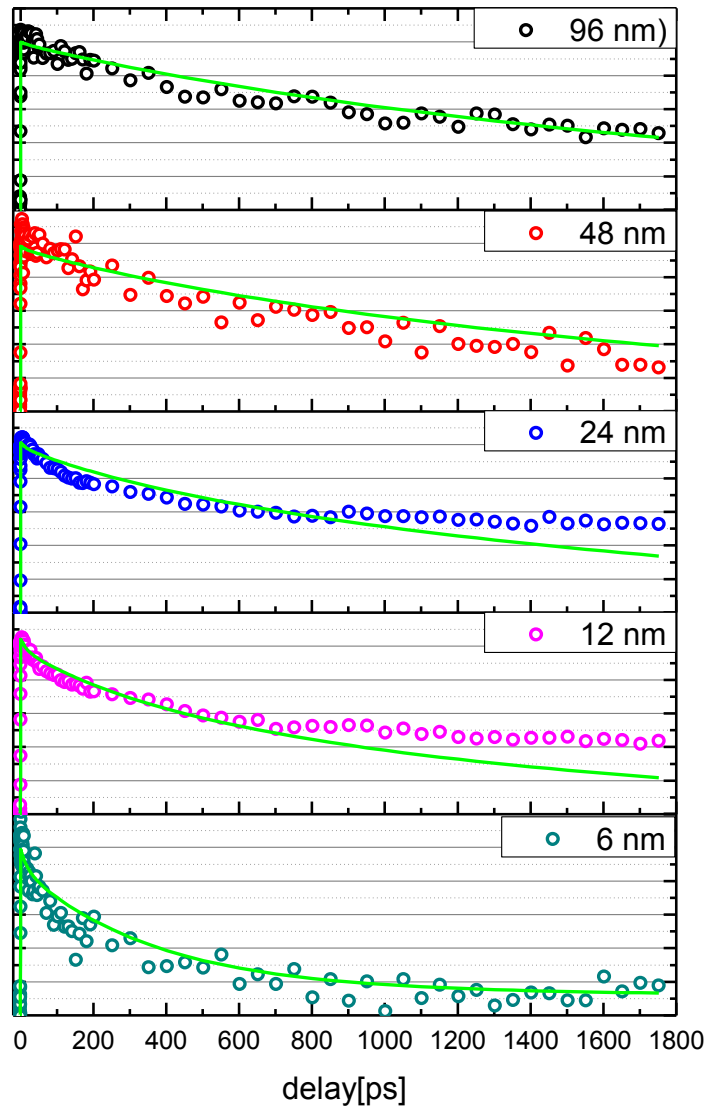


Figure 3.8 PIA experimental data with the correspondent fittings. The circles represent the experimental data points and the solid green lines stand for fits according to equation (25) convoluted with Gaussian apparatus function. All transients are normalized to their maxima. Excitation and probe wavelengths were set at 520 nm and 1.3 μm , respectively

As can be seen from Figure 3.8, the fitted curves show a reasonable level of consistency with the PIA experimental data with the 0-0.5 ns time scale. However, on a longer time scale, the model only works well for the thinnest and thickest sample and shows substantial deviations from the experimental results. Firstly, for the thinnest sample, the dynamics are dominated only by interfacial exciton dissociation. Then, for the 48 nm and 96 nm samples, the dynamics are mainly from the bulk exciton response. These effects are quite straightforward and can be directly simulated by the model. However, some unaccounted processes likely affect the dynamics of 12 nm and 24 nm samples, as discussed above.

The diffusion coefficient of vacuum-evaporated TV38 film was obtained by fitting

the experimental data as $D=7.7\times 10^{-5}$ cm²/s, and the exciton lifetime as $\tau=2.3$ ns. Therefore the diffusion length can be calculated with the following expression for the 3D diffusion [91]:

$$L = \sqrt{6D\tau} \quad (26)$$

The calculated exciton diffusion length is $L=10$ nm. This value is very well in line with the diffusion lengths in common organic materials [32, 33]. Note that the light penetration depth of TV38 layer was estimated to be 80 nm which is much higher than this exciton diffusion length. Therefore, a large fraction of absorbed photons are able to convert into excitons however cannot make it to reach the interface thus recombines within the exciton life time. This conflict between exciton diffusion distance and light penetration depth must be resolved in the future designing of devices. For example, Increase the molecular ordering in the films will increase the exciton diffusion distance, therefore optimization can be done with this factor.

3.5 Conclusion

The exciton diffusion in vacuum-deposited TV38 layers sandwiched between the C₆₀ electron accepting layers were studied by absorption spectroscopy and time-resolved PIA spectroscopy. Vacuum-deposited TV38 molecules demonstrate wide and prominent absorption bands, which is an inspiring feature of an OSC material.

The exciton dynamics in TV38 layers were studied by ultrafast PIA spectroscopy and Exciton described by an analytical model. According to the model, exciton diffusion length was estimated to be around 10 nm, which is rather limited compared to the light penetration depth (~80 nm). Therefore, in order to increase the exciton diffusion length to achieve better balanced between exciton diffusion length and light penetration depth, we need to further optimize the molecular packing and crystallinity of the vacuum-deposited film. However, the analytical model was not fully succeeded in describing the dynamics of the intermediate samples with thickness of 12 nm and 24 nm, which is most probably caused by the complicated interplay between exciton and polaron dynamics.

The relatively low exciton diffusion length may results in a low current for the layered solar cells [10]. To overcome this problem for TV38 molecule, the bulk heterojunction architecture can be employed to acquire a high light-to-charge conversion efficiency as discussed in the previous chapter. The diffusion length, in turn, can be potentially increased by improving the film packing properties in the vacuum-deposited layers.

3.6 Experimental

3.6.1 Sample preparation

In order to track the exciton diffusion process in TV38 layers, vacuum-evaporated samples were manufactured by the group of Prof. Jerome Cornil, University of Mons, Belgium. Layers of TV38 (figure 3.1a) with variable thickness (6-96 nm) were sandwiched between two 20 nm layers of C₆₀ fullerene (figure 3.1b). C₆₀ fullerene was chosen due to its relatively low absorption at 560 nm excitation wavelength, which allows us to maximize the optical contrast between C₆₀ and TV38 and selectively excite only the TV38 layer. Reference samples without C₆₀ layers with same layer thicknesses were also made on glass substrate. A C₆₀ layer with 40 nm thickness was also manufactured to examine the neat C₆₀ response.

For the experimental methods, see Chapter 2.

4. General Conclusions and Outlook

Organic solar cells (OSCs) are perspective alternative to conventional inorganic solar cells. Instead of employing inorganic material as active layer, OSCs feature an organic light-to-electricity converting materials. The main advantages of organic material for OSCs manufacturing are the solution processability which lead to a potentially inexpensive large volume production, lightweight and flexibility which result in a wide applicability in portable and wearable products. The main disadvantage of organic material which significantly limits the development of OSCs is relatively low light-to-charge conversion efficiency (13%) Therefore the urgent demand of discovering new materials has been a major concern and inspiration of OSC researchers.

This thesis is focused on studying of initial charge dynamics in a novel conjugated asymmetry molecule on an ultra-fast time scale. The initial dynamics are chosen because that all the charge generation processes in OSCs start from these initial dynamics, including exciton diffusion, exciton dissociation, charge generation and recombination. If there is no sufficient charge generated in the initial stage, nothing will help in the whole OSC efficiency. Therefore the initial dynamics play a key role in determining the overall efficiency, therefore are very important to investigate and interpret in order to design a material with sufficient initial charge generation. The *intra*-molecular (within a molecule) and *inter*-molecular (between neighboring molecules) charge transfer processes are identified and discussed, and also the main charge recombination channels are revealed that limit the long-lived charge generation efficiency.

This thesis is devoted to studying the photophysical properties of a new synthesized small molecule TPA-2T-DCV-Me (TV38) in OSC systems; the molecule was synthesized by the group of prof. S. Ponomarenko, Institute for Synthetic Polymer Materials, Moscow, Russia. This molecule was perspective candidate for efficient OSC donor material because of simplified synthesis, which was very promising for mass-scale production. The molecule was suitable both for solution processing and vacuum depositing, which enhances its applicability as donor material.

In this thesis, early-time exciton and charge dynamics in solution-processed BHJs and vacuum-deposited layers of TV38 have been investigated. The dynamics were studied by time resolved visible-pump IR-probe photoinduced absorption (PIA) spectroscopy technique. The experiments were conducted in such a way that the sample was first excited by an ultra-fast visible laser pulse, and the excited state dynamics were tracked by absorption of delay IR probe pulse. With the polarization sensitive setup arrangement, not only the isotropic (population) data, but also the anisotropy data (depolarization involved measurements) was tracked.

In chapter 2, charge dynamics studies of solution-processed bulk-heterojunctions thin

films based on TV38 were provided. The charges in BHJ blends with [70]PCBM acceptor were generated both via electron transfer from TV38 and hole transfer from [70]PCBM. The number of separated charges, however, was limited due to the *intramolecular* exciton recombination in the TV38 phase and/or recombination of interfacial charge-transfer states. The amount of long-lived separated charges depended strongly on the TV38:[70]PCBM ratio due to the balance between charge generation and recombination channels. With an optimal donor/acceptor blend ratio of 1:4, highest charge generation efficiency was observed and more than 50% of initially generated charge survived within the experimental time window of 2 ns. This offered important guidelines for the device engineering.

In chapter 3, exciton dynamics of TV38 in vacuum-deposited layered structure were demonstrated. By applying the vacuum-deposition method a good control of layer thickness was obtained (the vacuum-deposited samples were produced by the group of prof. Jerome Cornil, University of Mons, Belgium). From the exciton dynamics, relative low exciton diffusion distance of ~10 nm was obtained with an analytical model. On the other hand, at the maximum absorption wavelength, light penetration depth reaches an 80 nm length, which was indicative of a conflict between light penetration depth and exciton diffusion length. Therefore, low exciton diffusion distance might result in a low current for a solar cell system due to the limited exciton harvesting. However, vacuum-deposited sample might possess a different molecular stacking compare to the solution processed samples, which might introduce more inter-molecular interactions and potentially could increase the exciton diffusion length, however detailed explanation called for further study.

Base on the fact that the diffusion distance for TV38 is short, which would largely limit the layer thickness which in turn limits the light harvesting. Therefore BHJ architecture is a more promising choice for device designing for TV38 molecule. Nevertheless, there is another approach for device engineering. Since [70]PCBM has molecular symmetry which will lead to better molecular packing, thus a better exciton and charge diffusion distance can be achieved in the highly ordered [70]PCBM films, in this case, TV38 can be used as a hole acceptor, and the charge generation is mainly because of hole transfer processes. However the absorption cross section for [70]PCBM of sun light is relatively low, so large layer thickness is inevitable, then the advantage of better exciton diffusion distance is negatively compensated.

All in all, small molecules demonstrated outstanding and promising prospect for organic solar cell material designing. The reason is that they combined advantages of polymer such as solubility, broad absorption spectrum and flexibility, with the benefits of being small, more stable, suitable for vacuum-deposition and relatively easy to synthesis which lead to the probability of large volume production. However, for each molecule detailed optimization of the sample preparation procedure is required.

The methods described in this thesis provide important information both about the

intramolecular and *intermolecular* processes, therefore providing important insights both for synthetic chemists and device engineers.

5. Bibliography

1. Smil(2006), *P. 12*.
2. Morton, O., *Solar energy: A new day dawning?: Silicon Valley sunrise*. Nature, 2006. **443**(7107): p. 19-22.
3. Wikipedia. *Solar energy*. 2016 [cited 2016; Available from: https://en.wikipedia.org/wiki/Solar_energy.
4. University, S. *Exergy Flow Charts*. [cited 2016 27/03/2016]; Available from: <http://gcep.stanford.edu/research/exerycharts.html>.
5. Energypost. *Solar power passes 1% global threshold*. [cited 2016 27/03]; Available from: <http://www.energypost.eu/solar-power-passes-1-global-threshold/>.
6. García - Valverde, R., J.A. Cherni, and A. Urbina, *Life cycle analysis of organic photovoltaic technologies*. Progress in Photovoltaics: Research and Applications, 2010. **18**(7): p. 535-558.
7. Wolden, C.A., et al., *Photovoltaic manufacturing: Present status, future prospects, and research needs*. Journal of Vacuum Science & Technology A, 2011. **29**(3): p. 030801.
8. Avrutin, V., N. Izyumskaya, and H. Morkoç, *Semiconductor solar cells: Recent progress in terrestrial applications*. Superlattices and Microstructures, 2011. **49**(4): p. 337-364.
9. Tang, C.W., *Two - layer organic photovoltaic cell*. Applied Physics Letters, 1986. **48**(2): p. 183-185.
10. Rand, B.P. and H. Richter, *Organic Solar Cells: fundamentals, devices, and upscaling*. 2014: CRC Press.
11. Espinosa, N., et al., *Solar cells with one-day energy payback for the factories of the future*. Energy & Environmental Science, 2012. **5**(1): p. 5117-5132.
12. Lizin, S., et al., *The future of organic photovoltaic solar cells as a direct power source for consumer electronics*. Solar Energy Materials and Solar Cells, 2012. **103**: p. 1-10.
13. Tanaka, K. and Y. Chujo, *Recent progress of optical functional nanomaterials based on organoboron complexes with β -diketonate, ketoiminate and diiminate*. NPG Asia Materials, 2015. **7**(11): p. e223.
14. Liu, Z., et al., *Synthesis and characterization of novel polymers containing aminophenylsilole*. Polymer Journal, 2016.
15. Nakashima, M., et al., *Synthesis of silicon-or carbon-bridged polythiophenes and application to organic thin-film transistors*. Polymer Journal, 2016.
16. Rivers, P.N., *Leading Edge Research in Solar Energy*. 2007: Nova Science Publishers.
17. Saxman, A., R. Liepins, and M. Aldissi, *Polyacetylene: its synthesis, doping and structure*. Progress in polymer science, 1985. **11**(1): p. 57-89.
18. *The Nobel Prize in Chemistry 2000*. 2000 [cited 2016 29/03]; Available from: http://www.nobelprize.org/nobel_prizes/chemistry/laureates/2000/.
19. Heeger, A.J., *Nobel Lecture: Semiconducting and metallic polymers: The fourth generation of polymeric materials*. Reviews of Modern Physics, 2001. **73**(3): p. 681.
20. Zhang, J., et al., *Solution-Processable Star-Shaped Molecules with Triphenylamine Core and Dicyanovinyl Endgroups for Organic Solar Cells†*. Chemistry of Materials, 2010. **23**(3): p. 817-822.
21. Blom, P.W., et al., *Device physics of polymer: fullerene bulk heterojunction solar cells*.

- Advanced Materials, 2007. **19**(12): p. 1551-1566.
22. Yu, G., et al., *Polymer photovoltaic cells: Enhanced efficiencies via a network of internal donor-acceptor heterojunctions*. Science, 1995. **270**(5243): p. 1789.
 23. Kozlov, O.V., et al., *Ultrafast Charge Generation Pathways in Photovoltaic Blends Based on Novel Star - Shaped Conjugated Molecules*. Advanced Energy Materials, 2015. **5**(7).
 24. Brabec, C.J., N.S. Sariciftci, and J.C. Hummelen, *Plastic solar cells*. Advanced functional materials, 2001. **11**(1): p. 15-26.
 25. Brabec, C.J., et al., *Tracing photoinduced electron transfer process in conjugated polymer/fullerene bulk heterojunctions in real time*. Chemical Physics Letters, 2001. **340**(3): p. 232-236.
 26. Kim, J.Y., et al., *Efficient tandem polymer solar cells fabricated by all-solution processing*. Science, 2007. **317**(5835): p. 222-225.
 27. Cook, S., et al., *A photophysical study of PCBM thin films*. Chemical Physics Letters, 2007. **445**(4): p. 276-280.
 28. Cook, S., R. Kato, and A. Furube, *Ultrafast studies of charge generation in PCBM: P3HT blend films following excitation of the fullerene PCBM*. The Journal of Physical Chemistry C, 2009. **113**(6): p. 2547-2552.
 29. Wienk, M.M., et al., *Efficient methano [70] fullerene/MDMO - PPV bulk heterojunction photovoltaic cells*. Angewandte Chemie, 2003. **115**(29): p. 3493-3497.
 30. Koeppe, R. and N. Sariciftci, *Photoinduced charge and energy transfer involving fullerene derivatives*. Photochemical & Photobiological Sciences, 2006. **5**(12): p. 1122-1131.
 31. Bakulin, A.A., et al., *Ultrafast Hole - Transfer Dynamics in Polymer/PCBM Bulk Heterojunctions*. Advanced Functional Materials, 2010. **20**(10): p. 1653-1660.
 32. Markov, D.E., et al., *Accurate measurement of the exciton diffusion length in a conjugated polymer using a heterostructure with a side-chain cross-linked fullerene layer*. The Journal of Physical Chemistry A, 2005. **109**(24): p. 5266-5274.
 33. Haugeneder, A., et al., *Exciton diffusion and dissociation in conjugated polymer/fullerene blends and heterostructures*. Physical Review B, 1999. **59**(23): p. 15346.
 34. Mozer, A.J. and N.S. Sariciftci, *Conjugated polymer photovoltaic devices and materials*. Comptes Rendus Chimie, 2006. **9**(5): p. 568-577.
 35. Fischer, F.S.U., et al., *Highly Crystalline Films of PCPDTBT with Branched Side Chains by Solvent Vapor Crystallization: Influence on Opto-Electronic Properties*. Adv. Mater., 2014. **27**: p. 1223-1228.
 36. Kozlov, O.V., et al., *Real-Time Tracking of Singlet Exciton Diffusion in Organic Semiconductors*. Physical Review Letters, 2016. **116**(5): p. 057402.
 37. Halls, J., et al., *Efficient photodiodes from interpenetrating polymer networks*. 1995.
 38. Yu, G. and A.J. Heeger, *Charge separation and photovoltaic conversion in polymer composites with internal donor/acceptor heterojunctions*. Journal of Applied Physics, 1995. **78**(7): p. 4510-4515.
 39. Shaheen, S.E., et al., *2.5% efficient organic plastic solar cells*. Applied Physics Letters, 2001. **78**(6): p. 841-843.
 40. Peet, J., et al., *Efficiency enhancement in low-bandgap polymer solar cells by processing with alkane dithiols*. Nature materials, 2007. **6**(7): p. 497-500.
 41. Lanzani, G., *The photophysics behind photovoltaics and photonics*. 2012: John Wiley & Sons.

42. Günes, S., H. Neugebauer, and N.S. Sariciftci, *Conjugated polymer-based organic solar cells*. Chemical reviews, 2007. **107**(4): p. 1324-1338.
43. Dhanabalan, A., et al., *Synthesis and characterization of a low bandgap conjugated polymer for bulk heterojunction photovoltaic cells*. Advanced Functional Materials, 2001. **11**(4): p. 255-262.
44. Meier, H., *Conjugated oligomers with terminal donor–acceptor substitution*. Angewandte Chemie International Edition, 2005. **44**(17): p. 2482-2506.
45. Perzon, E., et al., *Design, synthesis and properties of low band gap polyfluorenes for photovoltaic devices*. Synthetic metals, 2005. **154**(1): p. 53-56.
46. Campos, L.M., et al., *Extended photocurrent spectrum of a low band gap polymer in a bulk heterojunction solar cell*. Chemistry of materials, 2005. **17**(16): p. 4031-4033.
47. KOZLOV, O.V., et al., *Ultrafast Intramolecular Dynamics in Novel Star-Shaped Molecules for Photovoltaic Applications*. Ultrafast Dynamics in Molecules, Nanostructures and Interfaces, 2014. **8**: p. 169.
48. Zhang, J., et al., *Solution-processable star-shaped photovoltaic organic molecules based on triphenylamine and benzothiadiazole with longer pi-bridge*. Organic Electronics, 2012. **13**(1): p. 166-172.
49. Kim, J., et al., *Push-pull organic semiconductors comprising of bis-dimethylfluorenyl amino benzo [b] thiophene donor and various acceptors for solution processed small molecule organic solar cells*. Solar Energy Materials and Solar Cells, 2012. **102**: p. 159-166.
50. Peumans, P., A. Yakimov, and S.R. Forrest, *Small molecular weight organic thin-film photodetectors and solar cells*. Journal of Applied Physics, 2003. **93**(7): p. 3693-3723.
51. Walker, B., C. Kim, and T.-Q. Nguyen, *Small molecule solution-processed bulk heterojunction solar cells†*. Chemistry of Materials, 2010. **23**(3): p. 470-482.
52. *Heliatek sets new Organic Photovoltaic world record efficiency of 13.2%*. Available from: <http://www.heliatek.com/en/press/press-releases/details/heliatek-sets-new-organic-photo-voltaic-world-record-efficiency-of-13-2>.
53. Sariciftci, N., et al., *Photoinduced electron transfer from a conducting polymer to buckminsterfullerene*. Science, 1992. **258**(5087): p. 1474-1476.
54. Heeger, A.J., *Semiconducting and metallic polymers: the fourth generation of polymeric materials*. The Journal of physical chemistry B, 2001. **105**(36): p. 8475-8491.
55. Mizrahi, U., et al., *Picoseconds time resolved photoinduced absorption by infrared active vibrations as a probe for charge photogeneration in MEH-PPV/C 60 composites*. Synthetic metals, 1999. **102**(1): p. 1182-1185.
56. Wei, X., et al., *Absorption-detected magnetic-resonance studies of photoexcitations in conjugated-polymer/C 60 composites*. Physical review B, 1996. **53**(5): p. 2187.
57. Österbacka, R., et al., *Excitons, polarons, and laser action in poly (p-phenylene vinylene) films*. The Journal of chemical physics, 2003. **118**(19): p. 8905-8916.
58. Müller, J.G., et al., *Ultrafast dynamics of charge carrier photogeneration and geminate recombination in conjugated polymer: fullerene solar cells*. Physical Review B, 2005. **72**(19): p. 195208.
59. Gordon, R., *Molecular collisions and the depolarization of fluorescence in gases*. The Journal of Chemical Physics, 1966. **45**(5): p. 1643-1648.
60. Luponosov, Y.N., et al., *Effects of electron-withdrawing group and electron-donating core*

- combinations on physical properties and photovoltaic performance in D- π -A star-shaped small molecules.* Organic Electronics, 2016.
61. Min, J., et al., *Effects of oligothiophene π -bridge length on physical and photovoltaic properties of star-shaped molecules for bulk heterojunction solar cells.* Journal of Materials Chemistry A, 2014. **2**(38): p. 16135-16147.
 62. Luponosov, Y., *personal communication.* 2016.
 63. Sharma, G., et al., *Efficient bulk heterojunction photovoltaic devices based on diketopyrrolopyrrole containing small molecule as donor and modified PCBM derivatives as electron acceptors.* Organic Electronics, 2012. **13**(4): p. 652-666.
 64. So, S., et al., *Novel unsymmetrical push-pull squaraine chromophores for solution processed small molecule bulk heterojunction solar cells.* Solar Energy Materials and Solar Cells, 2012. **98**: p. 224-232.
 65. Li, Z., et al., *Solution Processable Rhodanine - Based Small Molecule Organic Photovoltaic Cells with a Power Conversion Efficiency of 6.1%.* Advanced Energy Materials, 2012. **2**(1): p. 74-77.
 66. Shang, H., et al., *A Solution - Processable Star - Shaped Molecule for High - Performance Organic Solar Cells.* Advanced Materials, 2011. **23**(13): p. 1554-1557.
 67. Yin, B., et al., *Solution-processed bulk heterojunction organic solar cells based on an oligothiophene derivative.* Applied Physics Letters, 2010. **97**(2): p. 023303.
 68. Arbogast, J.W. and C.S. Foote, *Photophysical properties of C70.* Journal of the American Chemical Society, 1991. **113**(23): p. 8886-8889.
 69. Dennler, G., M.C. Scharber, and C.J. Brabec, *Polymer-fullerene bulk-heterojunction solar cells.* Adv. Mater, 2009. **21**(13): p. 1323-1338.
 70. Liu, Y., et al., *Solution - Processed Small Molecules Using Different Electron Linkers for High - Performance Solar Cells.* Advanced Materials, 2013. **25**(33): p. 4657-4662.
 71. Shi, Q., et al., *A Solution Processable D - A - D Molecule based on Thiazolothiazole for High Performance Organic Solar Cells.* Advanced Energy Materials, 2012. **2**(1): p. 63-67.
 72. Tamayo, A.B., B. Walker, and T.-Q. Nguyen*, *A low band gap, solution processable oligothiophene with a diketopyrrolopyrrole core for use in organic solar cells.* The Journal of Physical Chemistry C, 2008. **112**(30): p. 11545-11551.
 73. Lin, Y., et al., *A 3D star-shaped non-fullerene acceptor for solution-processed organic solar cells with a high open-circuit voltage of 1.18 V.* Chemical Communications, 2012. **48**(39): p. 4773-4775.
 74. Lin, Y., et al., *A star-shaped oligothiophene end-capped with alkyl cyanoacetate groups for solution-processed organic solar cells.* Chemical Communications, 2012. **48**(77): p. 9655-9657.
 75. Min, J., et al., *Alkyl Chain Engineering of Solution - Processable Star - Shaped Molecules for High - Performance Organic Solar Cells.* Advanced Energy Materials, 2014. **4**(5).
 76. Ripaud, E., et al., *Polarizability and Internal Charge Transfer in Thiophene-Triphenylamine Hybrid π -Conjugated Systems.* The Journal of Physical Chemistry B, 2011. **115**(30): p. 9379-9386.
 77. Deng, D., et al., *Solution-processable star-shaped photovoltaic organic molecule with triphenylamine core and thieno [3, 2-b] thiophene-dicyanovinyl arms.* Organic Electronics, 2012. **13**(11): p. 2546-2552.

78. Zapunidy, S.A., et al., *Approaches to low-bandgap polymer solar cells: Using polymer charge-transfer complexes and fullerene metallocomplexes*. Pure and Applied Chemistry, 2008. **80**(10): p. 2151-2161.
79. Sheng, C.-X., et al., *Experimental determination of the charge/neutral branching ratio η in the photoexcitation of π -conjugated polymers by broadband ultrafast spectroscopy*. Physical Review B, 2007. **75**(8): p. 085206.
80. Bakulin, A.A., et al., *Ultrafast charge photogeneration dynamics in ground-state charge-transfer complexes based on conjugated polymers*. The Journal of Physical Chemistry B, 2008. **112**(44): p. 13730-13737.
81. Kergoat, L., et al., *Use of poly (3-hexylthiophene)/poly (methyl methacrylate)(P3HT/PMMA) blends to improve the performance of water-gated organic field-effect transistors*. Organic Electronics, 2011. **12**(7): p. 1253-1257.
82. Dimitrov, S.D., et al., *On the energetic dependence of charge separation in low-band-gap polymer/fullerene blends*. Journal of the American Chemical Society, 2012. **134**(44): p. 18189-18192.
83. Kersting, R., et al., *Ultrafast field-induced dissociation of excitons in conjugated polymers*. Physical review letters, 1994. **73**(10): p. 1440.
84. Scharber, M. and N. Sariciftci, *Efficiency of bulk-heterojunction organic solar cells*. Progress in polymer science, 2013. **38**(12): p. 1929-1940.
85. Verreet, B., et al., *Improved cathode buffer layer to decrease exciton recombination in organic planar heterojunction solar cells*. Applied Physics Letters, 2013. **102**(4): p. 043301.
86. Kim, T.-M., et al., *Multilayer Epitaxial Growth of Lead Phthalocyanine and C70 Using CuBr as a Templating Layer for Enhancing the Efficiency of Organic Photovoltaic Cells*. ACS applied materials & interfaces, 2014. **6**(6): p. 4286-4291.
87. Österbacka, R., et al., *Two-dimensional electronic excitations in self-assembled conjugated polymer nanocrystals*. Science, 2000. **287**(5454): p. 839-842.
88. Mikhnenko, O., et al., *Temperature dependence of exciton diffusion in conjugated polymers*. The Journal of Physical Chemistry B, 2008. **112**(37): p. 11601-11604.
89. Theander, M., et al., *Photoluminescence quenching at a polythiophene/C 60 heterojunction*. Physical Review B, 2000. **61**(19): p. 12957.
90. Markov, D. and P. Blom, *Migration-assisted energy transfer at conjugated polymer/metal interfaces*. Physical Review B, 2005. **72**(16): p. 161401.
91. Mikhnenko, O.V., P.W. Blom, and T.-Q. Nguyen, *Exciton diffusion in organic semiconductors*. Energy & Environmental Science, 2015. **8**(7): p. 1867-1888.

6. Declaration

I declare that I have developed and written the enclosed Master Thesis completely by myself, and have not used sources or means without declaration in the text. Any thoughts from others or literal quotations are clearly marked. The Master Thesis was not used in the same or in a similar version to achieve an academic grading or is being published elsewhere.

Groningen, April 2016

Xiaomeng Liu